



Tartaric-sulphuric acid anodized clad AA2024-T3 post-treated in Ce-containing solutions at different temperatures: Corrosion behaviour and Ce ions distribution

Oscar Mauricio Prada Ramirez^{a,*}, Fernanda Martins Queiroz^{a,b}, Matheus Araujo Tunes^c, Renato Altobelli Antunes^d, Cleber Lima Rodrigues^e, Alex Lanzutti^f, Stefan Pogatscher^c, Marie-Georges Olivier^{g,h}, Hercílio Gomes De Melo^{a,*}

^a Escola Politécnica da Universidade de São Paulo, Av. Prof. Mello de Moraes, 2463 São Paulo, SP, Brazil

^b Escola e Faculdade de Tecnologia SENAI Suíço-Brasileira "Paulo Ernesto Tolle", R. Bento Branco de Andrade Filho, 379 São Paulo, SP, Brazil

^c Chair of Non-Ferrous Metallurgy, Montanuniversitaet Leoben, 18 Franz-Josef-Strasse, 8700 Leoben, Austria

^d Universidade Federal do ABC, Av. dos Estados, 5001 Santo André, SP, Brazil

^e Instituto de Física da Universidade de São Paulo, Rua do Matão, trav. R 187, 05508-090 São Paulo, Brazil

^f Polytechnic Department of Engineering and Architecture, University of Udine, Via del Cotonificio 108, 33100 Udine, Italy

^g Service de Science des Matériaux, Université de Mons, Place du Parc 23, 7000 Mons, Belgium

^h Materia Nova asbl, Avenue Copernic 1, 7000 Mons, Belgium

ARTICLE INFO

Keywords:

Aluminium
TSA
Ce post-treatment
Ce nanoreservoirs
S/TEM

ABSTRACT

The effect of temperature of a Ce-H₂O₂ post-treatment on the corrosion resistance of clad AA2024-T3 anodized in tartaric-sulfuric acid as well as the distribution of Ce oxyhydroxides in the anodized layer was investigated. Electrochemical impedance spectroscopy tests showed that samples post-treated at moderate temperatures (up to 50 °C) presented more stable and slightly higher impedance modulus than untreated ones. Increasing the post-treatment temperature to 75 °C decreased the corrosion resistance, likely due to damaging of the porous and barrier layer protective properties, as indicated by electric equivalent circuit fitting. Scanning electron microscopy characterization showed that Ce oxyhydroxides deposition (3+ and 4+ oxidation states as determined by X-ray photoelectron spectroscopy) was enhanced with increasing post-treatment temperature, and that pores were not blocked. Glow Discharge Optical Emission Spectrometry and Rutherford Backscattering Spectrometry analyses indicated local enrichment of Ce species at the bottom of the pores, whereas scanning transmission electron microscopy confirmed the presence of Ce-containing nanoparticles stuck to the pore's walls. Analyses of corroded samples showed increased amounts of Ce oxyhydroxides on the surface and that Ce species remained inside the pores, indicating that the post-treatment protocol successfully and durably incorporated Ce ions within the structure of the anodized layer.

1. Introduction

High mechanical strength Al alloys used in the aerospace industry have a complex microstructure due to thermomechanical treatments to which they are submitted, presenting intermetallics (IMs), dispersoids and hardening particles [1]. The presence of these particles, particularly IMs, generates local differences in the composition of the alloy and may cause microgalvanic effects leading to localized corrosion [2–4]. The high safety requirements of the aerospace industry demand that a robust corrosion protection system be employed. Currently, the aerospace industry standards employ Cr(VI)-containing compounds at all

stages of surface treatment [5]. This is justified by the active corrosion protection afforded by these compounds to the metallic substrate, favouring the regeneration of the oxide layer at defective sites through the reaction of hexavalent chromium ions leached from the protection system with species of the medium, a phenomenon known as self-healing [6,7]. However, hexavalent chromium compounds are harmful to health and to the environment, and their use is restricted or vetoed in several industrial sectors [8].

One of the most widely used methodologies to increase the corrosion resistance of Al and its alloys is anodizing. Briefly, the procedure consists in anodically thickening the Al oxide layer in a bath of suitable

* Corresponding authors.

E-mail addresses: oscarmprada@usp.br (O.M. Prada Ramirez), hgdemelo@usp.br (H.G. De Melo).

<https://doi.org/10.1016/j.apsusc.2020.147634>

Received 11 December 2019; Received in revised form 14 August 2020; Accepted 18 August 2020

Available online 24 August 2020

0169-4332/ © 2020 Elsevier B.V. All rights reserved.

composition. Anodizing in acid electrolyte results in an oxide with duplex structure, comprising a thick porous layer (few microns of thickness) and a thin barrier layer (few dozen nanometers) [9,10]. While the barrier layer provides a considerable increase in corrosion resistance, the open structure of the porous layer acts as an excellent base for the adhesion of organic coatings [11]. When the porous anodic layer is formed on pure or commercially pure Al, it exhibits a regular columnar structure [9,10]. However, the situation may dramatically change when the substrate is an Al alloy with complex microstructure, such as those of the 2XXX and 7XXX series. In these cases, incorporation of metallic or oxidized Cu particles in the oxide structure, triggering oxygen generation during the layer growth [12], and differences between the oxidation rates of the base matrix and the IMs [13–15], may lead to the development of a more defective oxide layer [16,17]. However, regardless of the substrate, the anodic layer must be further protected to ensure effective anticorrosion performance.

Chromic acid anodizing (CAA) is the benchmark in the aerospace industry. This procedure has been used for more than six decades, mainly in structural components [18]. The preference for CAA is justified by the self-healing properties provided by Cr (VI) compounds, giving excellent corrosion resistance, by the relatively low impact on the fatigue resistance of the parts and because the produced layer offers an excellent basis for painting application [19]. Tartaric-sulfuric acid (TSA), the electrolyte used in the present work, in addition to being considered environmentally friendly, according to some authors, results in anodized layers with corrosion resistance comparable to those produced in CAA [20]. According to some studies [21,22], the addition of tartaric acid to the sulfuric acid bath, while not significantly affecting the growth mechanism of the porous layer, reduces the anodizing current density. Presumably, this should lead to the formation of porous layers with lower thicknesses, which should positively affect the fatigue strength of the anodized alloy compared to the anodized material in sulfuric acid.

Anodized parts are usually stored prior to their use and topcoat application [5]. To protect the material against corrosion during this period, a primer layer is applied, which is also intended to serve as a link between the anodized substrate and the applied organic coating at the finishing step. The aerospace industry employs the commercial compound Alodine®, which contains Cr (VI) and F⁻, to produce a chemical conversion coating providing further protection of the substrate by the already mentioned self-healing properties [20]. Although this procedure shows recognized efficiency in the aerospace industry, as mentioned earlier, it poses risks to human health and the environment. Thus, there is a need to investigate the performance of environmentally friendly methodologies to replace the current technology.

Ce-based post-treatments relies among the most promising substitutes for Cr(VI)-based surface treatments for Al alloys [23]. The initial works on the corrosion protection of Al alloys by Ce-based corrosion inhibitors were performed by Hinton et al. [24–26]. They developed corrosion investigations of AA7XXX alloy in NaCl solution and verified that the addition of cerous cations could effectively reduce the corrosion rate of the alloy. The authors reported the precipitation of a Ce⁴⁺/Ce³⁺ oxyhydroxide film on the metal surface, the thickness of which increased with Ce ions concentration, immersion time and increased pH [25]. They also proposed an island growth mechanism for the protective layer, the driving force of which was the pH increase near cathodic sites, mainly IM particles, leading to the blockage of the cathodic reaction [25]. However, these initial works reported a relatively long immersion time to form a thick and protective conversion layer. This drawback was overcome by adding hydrogen peroxide to the conversion bath, which effectively reduced the treatment time to less than 10 min [27]. According to the literature [28] the addition of H₂O₂ to the conversion bath leads to the formation of complexes, such as Ce (H₂O₂)³⁺, which is followed by deprotonation, oxidation and precipitation of Ce oxyhydroxides.

Two main approaches have been used for obtaining corrosion

protection of Al alloys by means of Ce compounds: their direct application onto the substrate (conversion coatings, as those suggested by Hinton et al. [26,27] and the incorporation of Ce species into more complex protection systems. In the former approach the main sought effect is the blockage of surface-active sites (mostly cathodic ones), whereas in the latter the more sophisticated self-healing effect is the aim of the research [29–34]. In their seminal work about Ce conversion coatings production, by means of weight loss measurements, Hinton and Wilson [27] indicate that increasing the bath temperature did not significantly affect the protective properties of the coatings; however, a close examination of the presented plot (Fig. 5 in [27]) shows a slight but continuous decrease of the corrosion rate when the bath temperature was increased up to 70 °C. In another work, Dabala et al. [35] reported superior corrosion resistance of Ce-conversion coatings when the conversion bath temperature was raised to 50 °C. Even though particularities like alloy brand and conversion bath composition may be relevant for the determination of the optimized conditions for Ce conversion coatings application, several works investigating the corrosion behaviour of these coatings were performed at temperatures close to 50 °C [36,37], this seems to be a compromise between enhanced efficiency and extended bath life, as H₂O₂ is sensitive to thermal decomposition in aqueous solution. According to Bethencourt et al. [36] increasing the bath temperature favours the development of the alumina film over the metal matrix, improving the protective properties of the conversion layer. However, recent works also report enhanced anticorrosion properties for Ce-conversion coatings produced at room temperature (near 25 °C) [38,39]. Therefore, it seems that there is not a complete agreement in the literature about the ideal bath temperature for obtaining a Ce-conversion coating. Another relevant issue is that, to the best of the authors' knowledge, these conversion coatings were all obtained using Al alloys as substrate, which, due to their heterogeneous microstructure, offers ideal conditions for the island growth mechanism above cathodic IMs [25], increasing the efficiency of the process. This scenario differs from the one investigated in the present study, where the substrate is an anodic layer grown from a commercially pure aluminium substrate.

In the literature, only few works employed a post-treatment step using Ce salts to improve the corrosion protection of anodized Al alloys. The experimental procedures involve immersion of the anodized samples in Ce ions containing baths for varying times either at boiling temperature [11,40], in a procedure similar to the classical hydrothermal sealing, or at temperatures well below this value (ranging from room temperature to 50 °C) [41–46]. All studies reported that the Ce-based post-treatment enhanced the protective properties of the anodized layer, and some of them described improved or similar corrosion protection abilities when compared with chromate-based sealing procedures [11,41–43]. In the investigations performing post-treatments below the boiling point, H₂O₂ was added to the post-treatment bath to accelerate the oxidation of Ce³⁺ to Ce⁴⁺ [42–46], thus reducing the post-treatment time. The survey also showed that only some of these works presented SEM images of the samples surface [40,43–46], and, among them, only the micrographs presented by Prada-Ramirez et al. [45,46] clearly showed that the pores of the anodized layer were kept open after the Ce post-treatment step. Nevertheless, even in the works presenting no SEM characterization [11,41,42], there were clear references to pores sealing, indicating that they must have been plugged during the Ce post-treatment step.

As stated in the previous paragraph, the porous anodized layers post-treated in the Ce ions containing bath produced by Prada-Ramirez et al. [46] kept the pores open, thus maintaining the adhesion properties of the oxide layer aiming at future application of organic coatings. The authors investigated the effects of H₂O₂ concentration and immersion time in the corrosion protection by electrochemical impedance spectroscopy (EIS) and concluded that a more stable behaviour was obtained when the samples were immersed for two minutes in a 50 mM Ce(NO₃)₃ solution with the addition of 10% (w/w) H₂O₂. The

present work extends this research to evaluate the effect of the post-treatment bath temperature on the corrosion resistance of the anodized layer. Taking into account the literature findings [27,35–39] and that industrial hydrothermal sealing procedures are performed at temperatures close to the water boiling point for immersion times longer than 20 min, the chosen temperature range was 25–75 °C, maintaining the two minutes post-treatment determined by Prada-Ramirez et al. [46], in order to minimize the possibility of pore plugging. This latter feature is a differential of the present research when compared to most of the works using Ce-based post-treatment for corrosion protection of anodized Al alloys. It also focusses in the evaluation of Ce distribution on the sample surface and inside the pores of the anodized layer. A clad substrate was employed to allow better characterization of Ce distribution within the more defined pore structure of the anodized layer.

2. Experimental

2.1. Material and treatments

The clad AA2024-T3 sheet, with clad nominal composition: 0.3 wt% Si, 0.4 wt% Fe, 0.1 wt% Cu, 0.05 wt% Mn, 0.05 wt% Mg, 0.1 wt% Zn, 0.03 wt% Ti and 0.03 wt% others and balance of Al, was provided by an industrial partner. Microstructural characterization of the clad layer (not presented) showed the presence of Fe-Si IMs sparsely distributed on the surface [45].

Prior to anodizing, as-received specimens with dimensions (6.0 × 4.5 × 0.105) cm were degreased by sonication in acetone for 10 min. Surface treatment was performed by dipping the samples in an alkaline etching solution: NaOH (40 g L⁻¹) at 40 °C for 30 s and in a chromate-free commercial acid desmutting bath (Turco® Smuttgo-Henkel) at room temperature for 15 s. Between each step and at the end of the surface preparation procedure, the specimens were thoroughly washed for 5 min with distilled water.

Anodizing was carried out according to procedures already employed by our group by applying a constant voltage of 14 V for 20 min to the samples immersed in a TSA bath (40 g L⁻¹ H₂SO₄ + 80 g L⁻¹ C₄H₆O₆) maintained at 37 °C [46–48]. After anodizing, the samples were rinsed with deionized water and then post-treated for 2 min in a 50 mM Ce(NO₃)₃·6H₂O + 10% v/v H₂O₂ aqueous solution at different temperatures: (25 ± 2)°C (Ce10P 25C 2M); (50 ± 2)°C (Ce10P 50C 2M) and (75 ± 2)°C (Ce10P 75C 2M). The post-treatment conditions, as well as the acronyms that will be used to identify the samples throughout the text, are summarized in Table 1.

2.2. EIS characterisation

The corrosion behaviour of samples as-anodized (UNS) and post-treated in the Ce-H₂O₂ bath at different temperatures was evaluated using EIS in NaCl solution for 10 weeks (1680 h). In the first 5 weeks (840 h), the concentration of the electrolyte was 0.1 M, which was then increased to 0.5 M until the completion of the tests. This procedure was adopted due to the stability of the EIS response of most of the samples. Prior to each EIS experiment, the stability of the open circuit potential (OCP) was checked for about 10 min. Moreover, after increasing the electrolyte concentration (0.1 M to 0.5 M), to allow the system stabilization, a 24 h interval was given before the next EIS experiment.

Table 1
Post-treatments conditions and their acronyms.

Condition	Ce(NO ₃) ₃ ·6H ₂ O, mM	H ₂ O ₂ , % v/v	Temperature, °C	Time, min
UNS				
Ce10P 25C 2M	50	10	25	2
Ce10P 50C 2M	50	10	50	2
Ce10P 75C 2M	50	10	75	2

Differently from the initial work developed by Prada-Ramirez et al. [46], the samples were exposed in the vertical position, avoiding the deposition of corrosion products and improving reproducibility.

A three-electrode cell comprising the anodized piece (3.14 cm² of exposed area), an Ag/AgCl reference electrode and a platinum sheet (approximately 15 cm²) counter electrode was employed. A Potentiostat/Galvanostat/ZRA Gamry reference 600 + was used for the measurements. The frequency range was 10⁵ Hz to 10⁻² Hz, and the amplitude of the ac signal was 15 mV (rms) with an acquisition rate of 7 points per decade. For verifying reproducibility, measurements were performed at least in triplicate. The diagrams were fitted using Electric Equivalent Circuits (EECs) by means of the software Zview®. For the fitting procedure, only stable points were considered.

2.3. Morphological and compositional characterization

The morphological characterization of as prepared and EIS-tested samples was carried out by scanning electron microscopy (SEM) with field emission gun – FE-SEM - Inspect 50, equipped with secondary and backscattered electron detectors, and with facilities for energy dispersive X-ray analysis (EDS).

The oxidation state of the Ce species in the layers was determined using a ThermoFisher Scientific XPS spectrometer, k-alpha + model. The equipment operates with an Al-k-alpha monochromatic radiation source. The pressure in the analysis chamber was approximately 10⁻⁷ Pa. Narrow scan spectra were obtained in the Ce3d region. To evaluate the chemical state of Ce, the experimental curves were adjusted using the Avantage software using a Smart algorithm. Surface distribution maps were also acquired using this technique. The analysed area was approximately 20 mm², using a spot size of 30 μm.

The thicknesses of the anodized layers generated in TSA were determined using Glow Discharge Optical Emission Spectrometry (GDOES) using a Horiba Jobin Yvon profiling instrument at a pressure of 650 Pa and power of 35 W with a Cu anode of 4 mm in diameter. The instrument is equipped with a Runge Paschen polychromator, with 28 acquisition channels. The method of analysis was “sputtering rate”, calibrated using 20 different standards (Certified Reference Materials (CRM) and Setting Up Samples (SUS)). The measurements were performed following qualitative graphs and stopped when the erosion reached the substrate. This technique was also useful to evaluate the Ce distribution within the pores of the anodized layer.

Rutherford Backscattering Spectroscopy (RBS) was used to determine the presence of Ce species on the surface and within the pores of as-prepared anodized samples (Ce10P 50C 2M) and after 15 days immersion in 0.1 M NaCl (to accelerate the corrosion process, the sample was exposed horizontally). The spectra were obtained using an electrostatic accelerator (Pelletron-tandem, model 5SDH built by NEC) of the Laboratory of Analysis of Materials by Ionic Beams of the University of São Paulo (LAMFI-USP), with a He ion beam with energies of 3.8 and 4.4 MeV. The backscattered ions were measured with two surface-barrier detectors positioned at 120° and 170°. The adjustment was performed using simultaneous analysis of all the experimental data using the MultiSIMNRA [49] software with SIMNRA 7 [50] software for physics simulation, thus obtaining the multielemental depth profile.

2.4. Scanning transmission electron microscopy (S/TEM) characterization

Electron-transparent lamella from bulk clad AA2024-T3 anodized and Ce post-treated specimen was prepared using a conventional focused ion beam (FIB) technique for transmission electron microscopy (TEM) sample preparation [51]. A FEI Versa 3D dual beam Scanning Electron Microscope (SEM) and Ga + FIB operating a field emission gun (FEG) at 30 keV was used for electron-transparent sample preparation. In order to protect the surface of the bulk specimen from either Ga contamination or FIB induced-damage, a 2.25 μm Pt layer was deposited onto the surface prior the trenching and milling stages [52]. After attaching the lamella into a 3-post Gatan Omniprobe Mo grid, the specimen was polished (using cleaning cross-section patterning) up to a thickness of approximately 70 nm as constantly monitored by the electron beam within the SEM.

The electron-microscopy characterization of the FIB-produced electron-transparent lamella was carried out in a ThermoFisher Scientific™ Talos F200X G2 transmission and scanning transmission electron microscope (STEM) operating a X-FEG at 200 keV. Prior the characterization, the sample was subjected to Ar plasma cleaning for 5 min. The characterization was performed using both the TEM mode, with bright-field TEM (BFTEM) and selected-area electron diffraction (SAED), and in STEM mode, with the high-angle annular dark field (HAADF) and bright-field (BF) detectors. The spatial resolution of the STEM-HAADF mode is around of 0.14 nm. This microscope is also equipped with Super-X energy dispersive X-ray (EDX) spectroscopy which was also used in this work for analysing the cross-sectional line profiles and elemental distribution along the electron-transparent lamella. Quantification of the STEM-EDX results was performed both in the ThermoFisher Velox and the ImageJ [53] softwares.

3. Results and discussion

3.1. EIS behaviour

Bode plots for clad AA2024-T3 anodized in TSA are shown in Figs. 1–4 for samples UNS, Ce10P 25C 2M, Ce10P 50C 2M and Ce10P 75C 2M, respectively. As previously explained, samples were exposed to NaCl 0.1 M for 5 weeks (840 h), and then the concentration was increased to 0.5 M up to the end of the experiment, totaling 10 weeks (1680 h). Overall, the low frequency (LF) impedance modulus remained stable with immersion time, except for the Ce10P 75C 2M sample (Fig. 4), which showed a steady decrease of the impedance modulus from 672 h of immersion. However, independently of the LF behaviour,

from 168 h onwards, there is a progressive increase of the impedance modulus in the high (HF) to medium (MF) frequency domain. This response coincides with the onset of a new time constant in the HF range, which becomes more defined and capacitive (higher phase angles) as time elapses. For anodized Al, this response is associated with physicochemical phenomena taking place inside the pores, leading to their sealing and resulting in a greater difficulty to current flow, thus increasing the impedance modulus in this frequency range [46–48,54–56].

The analysis of the phase angle diagrams offers a clear picture of the changes occurring in the anodized layer due to the interaction with the test electrolyte. For short immersion times, the pores are open and filled with the conductive solution. Thus, the interface response consists of a single capacitive time constant that characterizes the barrier layer properties. The phase angle, close to 90° in the whole frequency range, associated with the high LF impedance modulus, reflects the good protective properties of this layer [11]. As immersion time increases, aluminium oxyhydroxides and corrosion products precipitate inside the pores [55], progressively blocking them, a process denominated self-sealing [54]. This imposes a resistance to current flow through the pores and a new capacitive time constant develops in the HF domain. With increased precipitation and stronger pore blockage, this time constant becomes better resolved and more capacitive [54], and the impedance modulus in the HF region increases. However, for less protective systems, as the one presented in Fig. 4 (Ce10P 75C 2M), these changes take place earlier. As shown in Fig. 4, two-time constants are visible since the early immersion times, indicating precipitation inside the pores. Moreover, the separation between the time constants is less evident, pointing to overlapping phenomena. Therefore, for this particular sample, the post-treatment seems not to be effective, and aggressive species may reach the barrier layer resulting in increased corrosion activity and earlier failure.

The Nyquist plots of the samples have similar shapes (data not presented), indicating that the corrosion process is alike for all of them. In such cases, the LF impedance modulus can be used to compare the corrosion resistance of the samples [44,57–59]. Fig. 5 displays the evolution of the LF (10 mHz) impedance modulus with immersion time for the UNS sample and for the samples post-treated in the Ce-H₂O₂ containing bath at different temperatures. Error bars were included for each measurement to demonstrate reproducibility. Besides confirming the worst performance of the sample post-treated at 75 °C (Ce10P 75C 2M), already evident in the Bode plots, the Figure shows that throughout the test period, the Ce10P 50C 2M and Ce10P 25C 2M samples presented more stable behaviours than the UNS sample and

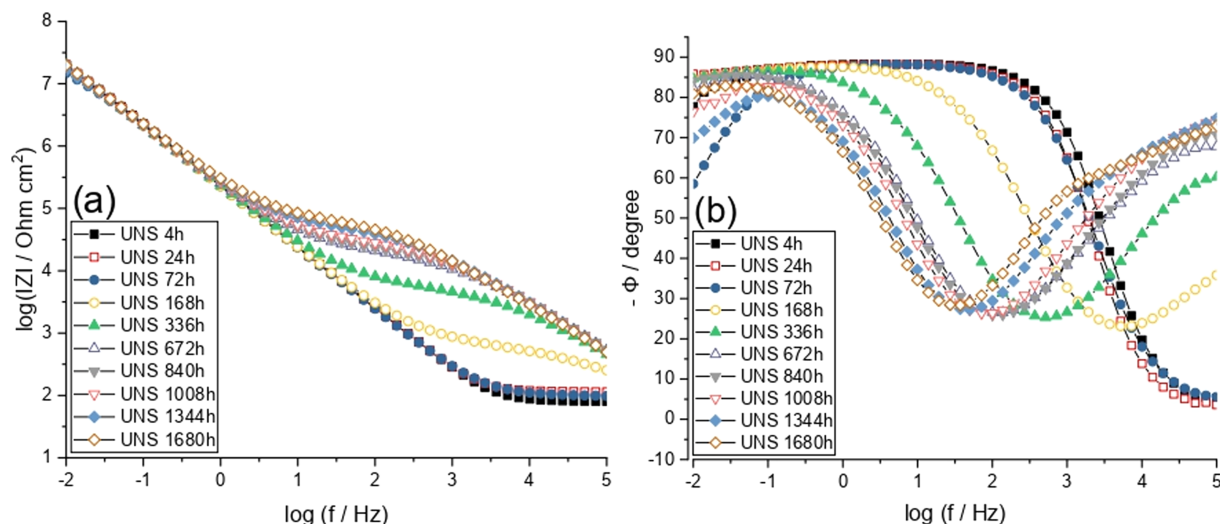


Fig. 1. Bode plots in 0.1 M NaCl (4 h – 840 h) and 0.5 M NaCl (840 h – 1680 h) solution of Alclad AA2024-T3 anodized in TSA (UNS).

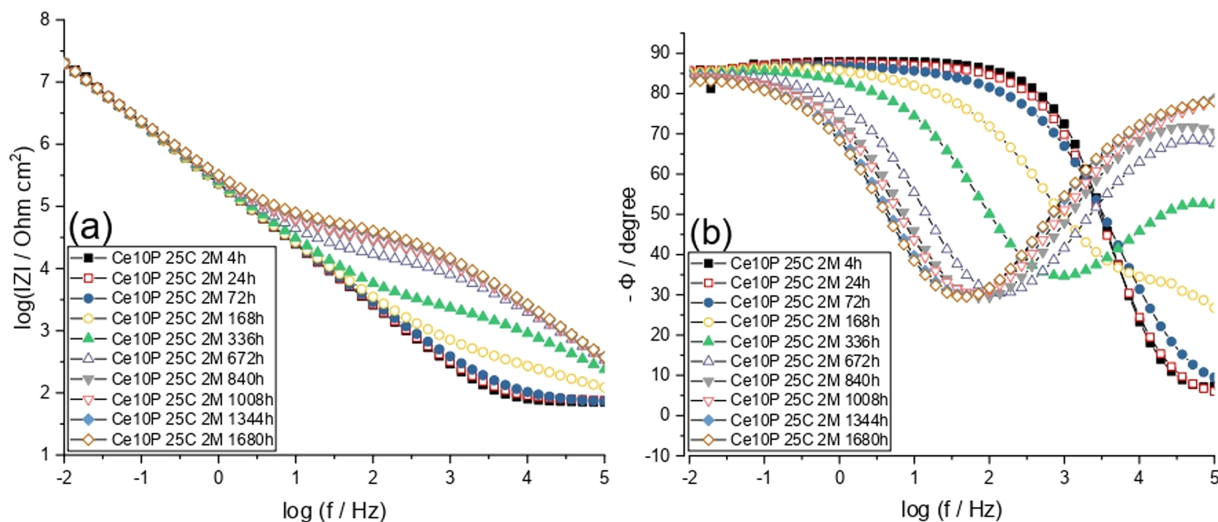


Fig. 2. Bode plots in 0.1 M NaCl (4 h – 840 h) and 0.5 M NaCl (840 h – 1680 h) solution of Alclad AA2024-T3 anodized in TSA and post treated in 50 mM Ce (NO₃)₃ and H₂O₂ (10% v/v) for 2 min at 25 °C (Ce10P 25C 2M).

similar LF impedance modules, with a small differentiation between them in the tests performed after 1344 h, at which the impedance modulus was slightly higher for the sample post-treated at 50 °C.

Fig. 6 shows the EECs used to fit the EIS diagrams of the UNS sample and of the samples post-treated at different temperatures in the bath containing Ce-H₂O₂. They are similar to others employed in the literature for anodized Al [46,47,60], and the different proposed schemes consider the evolution of the interface with immersion time. The EEC of Fig. 6(a) was used to fit the diagrams from 4 to 72 h of most samples. In this period, the pores of the porous layer were still open; thus, it comprises the solution resistance (Rs) in series with the response of the barrier layer (Rb and CPEb) at the pores bottom. After 168 h of test, enough precipitation had occurred inside the pores promoting their partial sealing; therefore, another time constant was added (CPEp and Rp) to consider this phenomenon (Fig. 6(b)). Finally, the EEC of Fig. 6(c) was employed to fit the data from 336 h until the end of the experiments. In this EEC, a parallel capacity (Cpw-capacity of the pore walls) was added to the EEC of Fig. 6(b) to take into account the deterioration of the porous layer and the increase of the Rp parameter, which imposes increased resistance for the current to flow through the blocked pores. Physically, the capacitance of the pore walls (Cpw) in

Fig. 6(c) must display a parallel resistive pathway (Rpw), corresponding to the resistance of the pore walls, as proposed by Gonzales et al. [54]; however, the resistive response of the porous layer is too high when compared with the other resistive elements, and no current must pass through this element [61]. Therefore, as Rpw is not detected by the impedance measurement, it was omitted from the EEC model representation.

The variation in the resistance of the barrier layer (Rb) and of the corrosion products precipitated inside the pores (Rp) (partial sealing) as a function of immersion time is presented in Fig. 7(a) and 7(b), respectively. For the samples with stable corrosion behaviour (UNS, Ce10P 25C 2M and Ce10P 50C 2M), Rb is about four orders of magnitude higher than Rp, confirming that the barrier layer is the main responsible for the corrosion resistance [11]. These samples also showed fairly stable Rb values until the end of the test, indicating that aggressive species fail to damage the protective properties of this layer. In accordance with the overall corrosion performance presented in Fig. 5, the Ce10P 50C 2M sample presented slightly higher Rb values throughout the test time, indicating better performance. In turn, Rb for the Ce10P 75C 2M sample showed a very unstable behaviour and effectively failed when the NaCl concentration was increased from 0.1 M

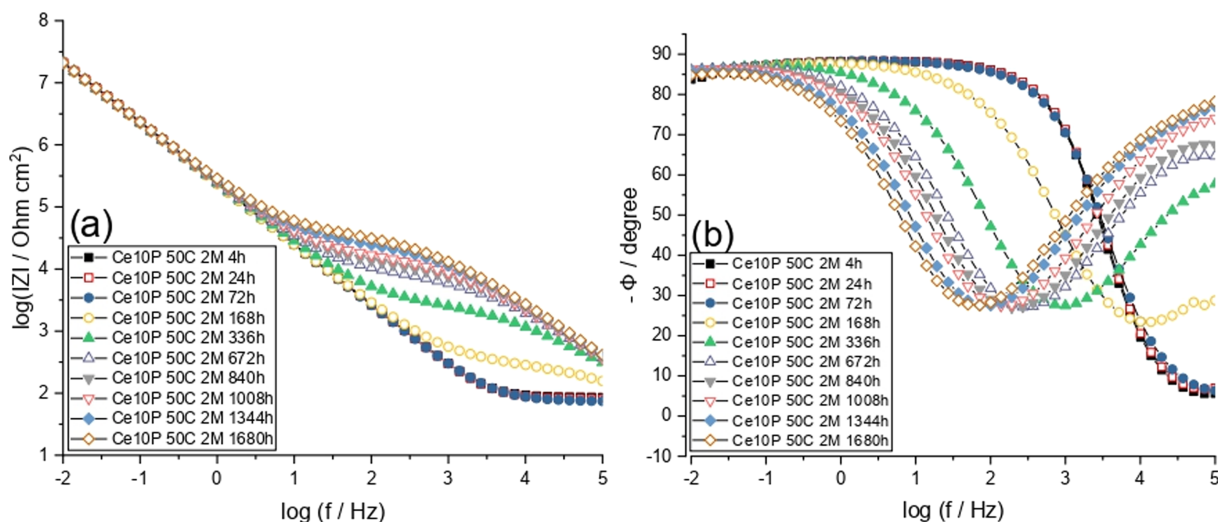


Fig. 3. Bode plots in 0.1 M NaCl (4 h – 840 h) and 0.5 M NaCl (840 h – 1680 h) solution of Alclad AA2024-T3 anodized in TSA and post treated in 50 mM Ce (NO₃)₃ and H₂O₂ (10% v/v) for 2 min at 50 °C (Ce10P 50C 2M).

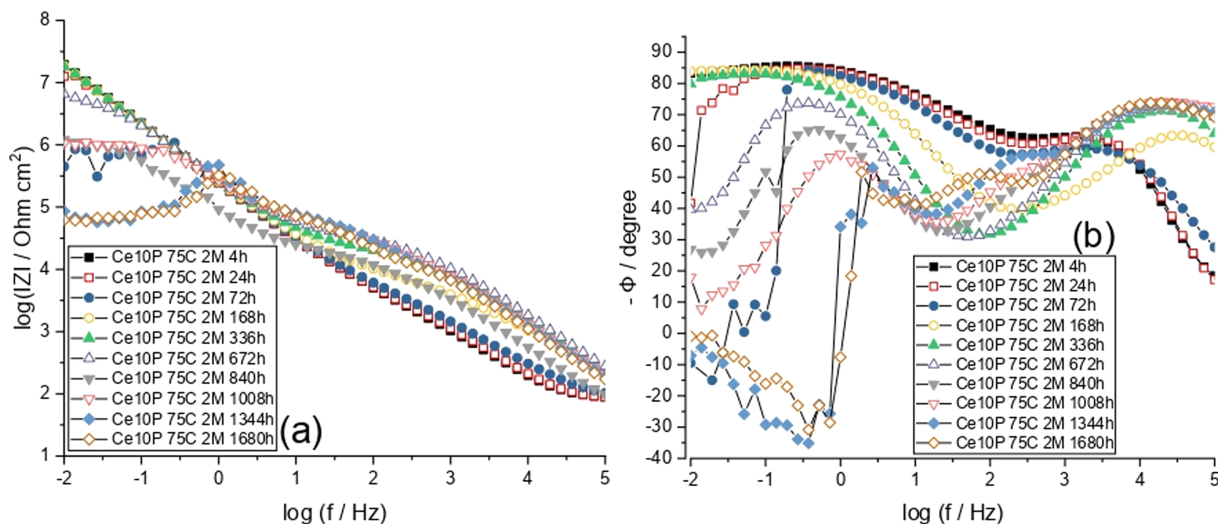


Fig. 4. Bode plots in 0.1 M NaCl (4 h – 840 h) and 0.5 M NaCl (840 h – 1680 h) solution of Alclad AA2024-T3 anodized in TSA and post treated in 50 mM Ce (NO₃)₃ and H₂O₂ (10% v/v) for 2 min at 75 °C (Ce10P 75C 2M).

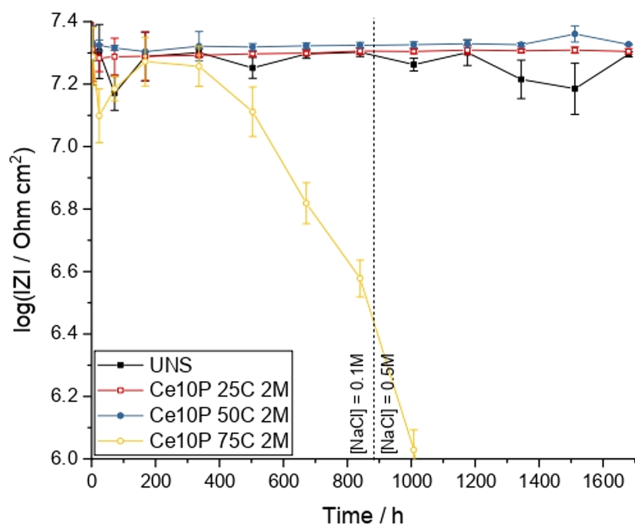


Fig. 5. Evolution of the impedance modulus at 10 mHz with immersion time in 0.1 M NaCl (4 h – 840 h) and 0.5 M NaCl (840 h – 1680 h) of Alclad AA2024-T3 anodized in TSA, untreated (UNS), and post treated according to the different procedures. To the right of the vertical dotted line experiments were performed in 0.5 M NaCl. Error bars are included to demonstrate reproducibility.

to 0.5 M. This indicates that this post-treatment was detrimental to the integrity of the barrier layer, as it presented a far worse response than the UNS sample.

Similar Rp behaviours were observed for all the samples (Fig. 7(b)). An increase with immersion time was verified, indicating permanent precipitation of aluminium oxyhydroxides/corrosion products inside the pores and increased blockage to current flow [46,54]. Interestingly, the sample with the worst corrosion resistance presented the higher Rp values, indicating that this parameter cannot be used to evaluate the anticorrosion performance. As presented later, SEM characterization of the Ce10P 75C 2M sample after the post-treatment showed large amounts of Ce precipitates, pointing to an excessive attack of the porous layer. This result is similar to that obtained previously, at which an excess immersion time, 20 min, in the bath containing Ce ions and 10% H₂O₂ led to the deterioration of the corrosion resistance of the anodized sample [46], and confirms that excessive interaction with the Ce-H₂O₂ solution, characterized either by longer post-treatment periods [46] or excessively high temperatures (in the present case 75 °C), impairs the corrosion protection of the anodized layer. The joint analysis of the results presented in this paragraph and in the previous one allows us to assume that the integrity of the anodic layer of the sample post-treated at 75 °C was compromised during the post-treatment step.

Fig. 7(c) displays the evolution of the constant phase element associated with the barrier layer (CPEb). The fitting procedure showed “n” very close to 1 (most of them were superior to 0.95), indicating an almost perfect capacitive response. For the samples with stable corrosion behaviour: UNS, Ce10P 25C 2M and Ce10P 50C 2M, CPEb increased slightly in the early test times and then progressively decreased. The overall response indicates that the initial behaviour could be associated with progressive hydration (note that thinning could also cause this response; however, in this case, a continuous increase of the

(a)		4 – 72h	
		UNS, Ce10P 25C 2M, Ce10P 50C 2M	
(b)		168h	4 – 72h
		UNS, Ce10P 25C 2M, Ce10P 50C 2M,	Ce10P 75C 2M
(c)		336 – 1680h	168 – 1680h
		UNS, Ce10P 25C 2M, Ce10P 50C 2M,	Ce10P 75C 2M

Fig. 6. Electrical equivalent circuits (EECs) used to fit the EIS diagrams in 0.1 M NaCl (4 h – 840 h) and 0.5 M NaCl 840 h – 1680 h) of Alclad AA2024-T3 anodized in TSA untreated (UNS) and post-treated according to the different procedures. The immersion times at which each samples was employed for the different samples are also indicated.

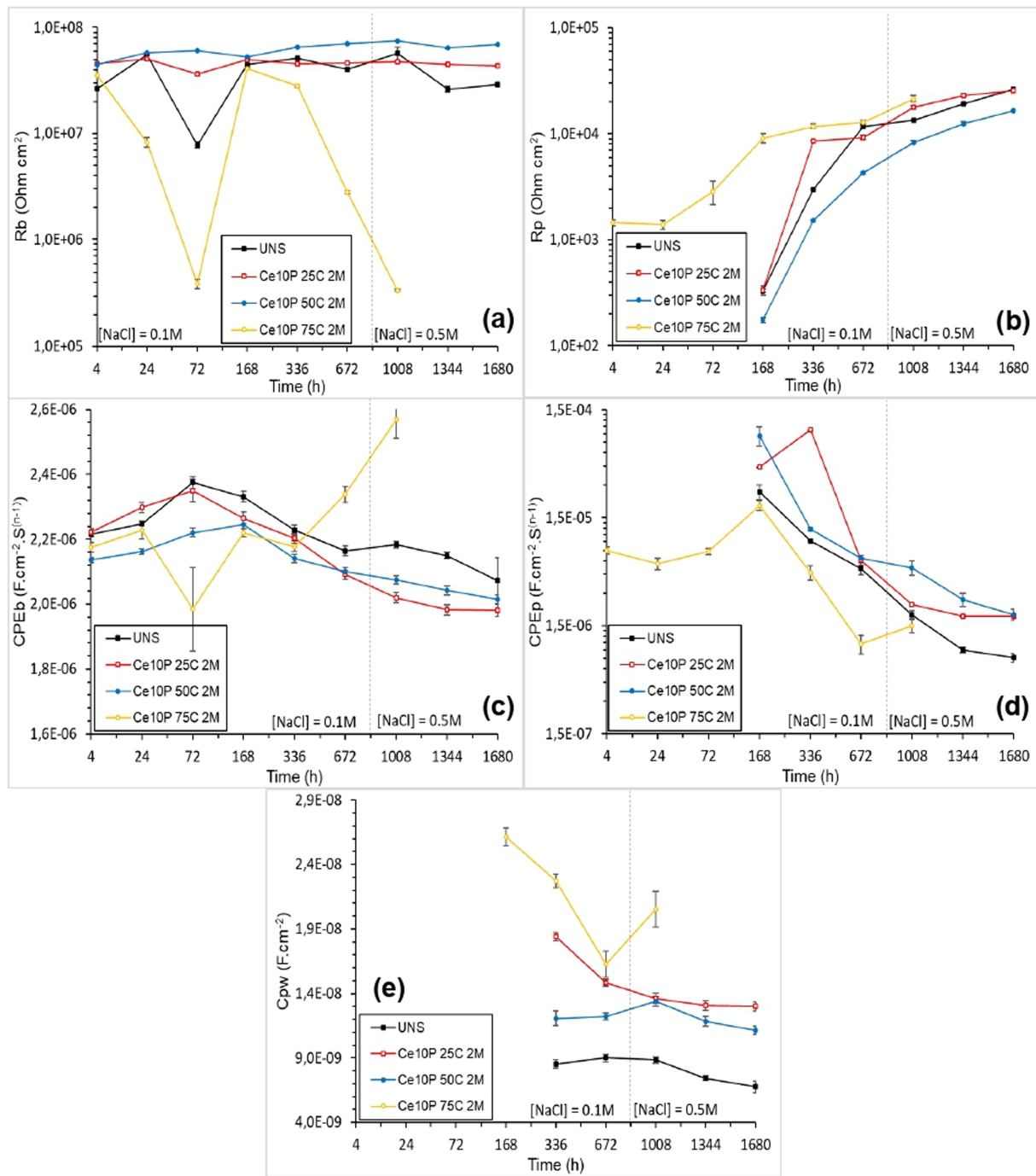


Fig. 7. Results of the fitting of the EIS diagrams with the EECs of Fig. 6 for the Alclad AA2024-T3 anodized in TSA bath, without (UNS) and after post-treatments: Ce10P 25C 2M, Ce10P 50C 2M, Ce10P 75C 2M, (a) Rb, (b) Rp, (c) CPEb, (d) CPEp (e) Cpw.

capacitance should be expected). The posterior decrease of CPEb indicates a positive interaction with the precipitated products inside the pores leading to an improvement in the capacitive response. In turn, for the Ce10P 75C 2M sample, a quasi-continuous increase of CPEb was observed until the sample failed, confirming the deleterious effect of the post-treatment at 75 °C to the protective properties of the barrier layer. Overall, CPEb was slightly lower for the Ce10P 25C 2M and Ce10P 50C 2M samples indicating a positive effect of the post-treatment step at these two temperatures.

The variation in CPEp was similar for all samples: the values decay with immersion time (Fig. 7(d)). This response is related to the self-sealing process, resulting in a progressive closure of the pores with

consequent increase of the difficulty to current flow, and is in agreement with the increase in the impedance modulus and in the capacitive behaviour in the HF and MF ranges observed in the EIS experiments. Overall, the CPEp and Rp responses suggest increased precipitation inside the pores for longer immersion times [46,54,62]. The exponents of CPEp were close to 0.5 (between 0.45 and 0.6). In the literature, this low exponent value has been associated to a transmission line model, in accordance with the porous nature of the anodized layer [61]. However, the de Levie model assumes that the walls of a porous electrode must be conductive and reactive [63,64], which is not the case for the aluminium oxide formed during the anodizing procedure, which is basically dielectric. Recently, Prada Ramirez et al. [46] suggested that

this CPE response could be associated with an in-depth distribution of the resistance and/or capacity of the precipitates inside the pores, in line with recent developments in the interpretation of the CPE response of oxides and protective layers [65,66], which, in our opinion, more realistically represents the phenomena taking place within the blocked pores.

Finally, as shown in Fig. 7(e), the capacity of the pore walls (Cpw) was fairly constant, indicating its stability. The fitted values are about three orders of magnitude lower than those found for the barrier layer (Fig. 7(c)) and are compatible with the thickness of the porous layer, as determined in other works [46,47,59]. Cpw was slightly higher for the samples post-treated in the Ce-H₂O₂ containing solution, indicating interaction with the post-treatment bath.

The differences between the corrosion behaviour of the samples post-treated at different temperatures may be related to the dissolution of the anodized layer in the post-treatment bath (pH = 3.08). As mentioned by Lin et al. [67] and Gordovskaya et al. [44], the first step in the formation of Ce conversion layers on anodized aluminium alloys is the dissolution of the oxide layer in the conversion bath according to reaction (1).



Fig. 8 displays SEM micrographs of as-produced UNS, Ce10P 25C 2M, Ce10P 50C 2M and Ce10P 75C 2M samples. They show the open pore structure already verified and discussed in another work [46] and evidence a strong precipitation of Ce oxide, confirmed by EDS analysis, when the post-treatment was performed at the highest temperature (Fig. 8(d)). According to Gordovskaya et al. [44], whichever reaction involved in the precipitation of Ce oxyhydroxides consumes hydroxyl ions. Therefore, increased Ce precipitation must decrease the interfacial pH, potentiating reaction (1), leading to a stronger dissolution of the anodized layer during the post-treatment step. However, a critical temperature threshold must exist for the increased Ce deposition and

oxide layer dissolution processes, as increasing the post-treatment bath temperature from 25 °C to 50 °C only slightly increased Ce oxide deposition, as shown in the inserts in Fig. 8(b) and 8(c), and did not hinder the corrosion resistance. Finally, it is important to stress that even though increased Ce oxyhydroxides deposition was verified for the Ce10P 75C 2M sample, which exhibited a faint yellow colour, the typical dry mud pattern associated with the Ce conversion layers was not observed, indicating that the Ce layer was much thinner than that reported by Gordovskaya et al. [44].

3.2. Investigation of the incorporation of Ce ions in the anodized layer

As already mentioned in the introduction, Ce-based post-treatments are among the most promising surface treatments to replace Cr(VI)-based procedures, and, frequently, the presence of Ce ions has been associated to self-healing abilities [29–34]. Although this specific feature is not investigated in the present work, it is important to verify the presence of Ce ions in the structure of the anodized layer before and after the corrosion tests.

3.2.1. Analyses of uncorroded samples

3.2.1.1. XPS characterization. The SEM images presented in Fig. 8 already demonstrated the precipitation of Ce oxyhydroxides on the samples surface during the post-treatment step; however, for samples Ce10P 25M 2M and Ce10P 50C 2M, only few dispersed spots presented sufficient Ce accumulation to be significantly analysed by EDS. Therefore, XPS analyses were performed to investigate the Ce oxidation state and its distribution on top of the anodized layer. The deconvoluted high-resolution XPS spectrum of Ce3d acquired on the as-prepared Ce10P 50C 2M sample (Fig. 9-sample with the best anticorrosion performance) is similar to others reported in the literature for Ce conversion layers [44,68,69]. According to Uhart et al. [69], the 10 peaks of the deconvoluted spectrum, the bindings energies (BE) of which are presented in Table 2, can be ascribed as

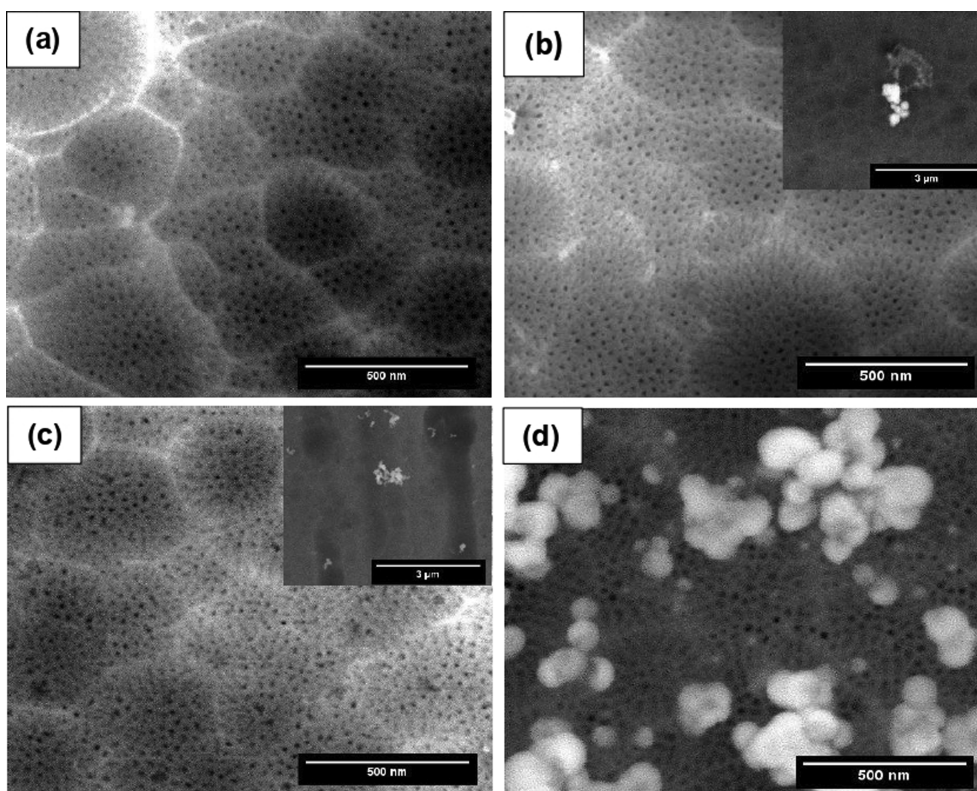


Fig. 8. SEM micrographs of the clad AA2024-T3 anodized in TSA bath: (a) as-produced (UNS) and after post-treatments, (b) Ce10P 25C 2M, (c) Ce10P 50C 2M, (d) Ce10P 75C 2M. The inserts in (b) and (c) show Ce oxide deposition.

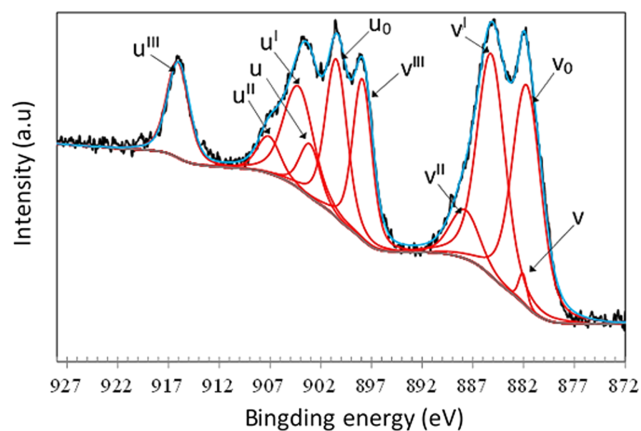


Fig. 9. Deconvoluted high resolution spectrum of Ce3d for the Ce10P 50C 2M sample.

follows: two doublets to Ce^{3+} (v_0-u_0 and $v'-u'$) and 3 doublets to Ce^{4+} (as $v-u$, $v''-u''$ and $v'''-u'''$). The authors also state that the peak u''' at a BE of 916.0 eV is considered a fingerprint of Ce^{4+} [69]. Table 2 also shows that the $\text{Ce}^{3+}/\text{Ce}^{4+}$ ratio extracted from the XPS spectrum is equal to 2.13, which is in good agreement with the results from Yu and Li [68], who reported increased amounts of Ce^{4+} species in the superficial layers due to oxidation upon exposure to the air. Gordovskaya et al. [44] reported much higher amounts of Ce^{4+} ions in their Ce conversion layers ($\text{Ce}^{3+}/\text{Ce}^{4+}$ ratio of about 0.45 for anodized layers produced under similar conditions to those reported in this work). However, in the work by Gordovskaya et al. [44], the post-treatment time was 30 min, as compared to 2 min in the present investigation, which must have increased the amount of Ce^{4+} ions in the bulk post-treatment solution [43,44]. Indeed, the XPS spectra acquired on samples post-treated for 5 min in the $\text{Ce}-\text{H}_2\text{O}_2$ solution for 5 min (data not presented) showed a decrease in the $\text{Ce}^{3+}/\text{Ce}^{4+}$ ratio (0.92), which was ascribed to increased oxidation of Ce^{3+} to Ce^{4+} in the bulk post-treatment bath, as indicated by its increased yellow hue. Therefore, the longer post-treatment time used by Gordovskaya's et al. [44] must explain the differences with the present work. Finally, note that the literature documents that Ce^{3+} ions are the main responsible for self-healing properties in corrosion protection systems for aluminium alloys [70]. Therefore, increased amounts of this ion in the Ce layer could favour self-healing properties when using this post-treatment step as a part of a more complex corrosion protection system (ongoing research).

The distribution map of Ce3d, O1s and Al2p on the surface of the Ce10P 50C 2M sample was also determined by XPS (Fig. 10), which was obtained from the individual elemental distribution maps displayed in Fig. 11. The aim of such representation is to give a visual indication of the sites where each element is encountered and its relative concentration over the analysed area, according to the scale bars shown at right of Fig. 10. It shows an almost homogeneous distribution of Ce over a large fraction of the analysed area, indicating that a very thin Ce oxyhydroxide layer may have precipitated on most of the surface. Conversely, as expected, the quantification of the atomic fraction of each element (Fig. 11) showed that the largest amount was associated to O1s, followed by Al2p from the anodized layer with Ce3d at a smaller quantity. The map in Fig. 11c reveals that the sites where Ce concentration is low (dark regions) are relatively few when compared to

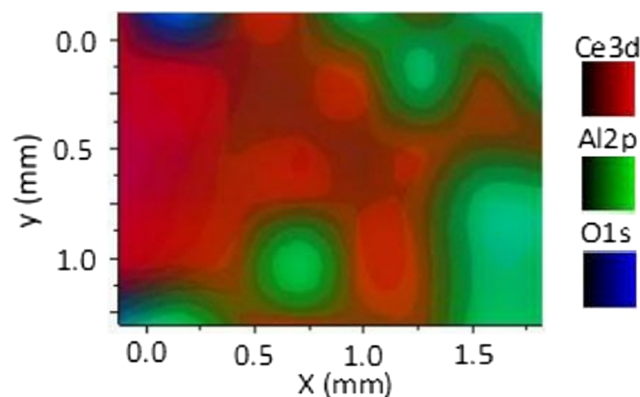


Fig. 10. XPS map showing the distribution of Ce3d, Al2p and O1s at the surface of Ce10P 50C 2M sample.

those where it is more intense. At these sites, Al and O predominate, as observed in Fig. 11a and 11b. Fig. 10 shows the overlaid image of these individual distributions.

3.2.1.2. GDOES analysis. Fig. 12(a) shows the GDOES depth profiles of the relevant species for the Ce10P 50C 2M sample. The aluminium concentration profile allows defining three regions: the first, with an approximately constant Al content (about 4.0- μm thick), corresponds to the thickness of the porous oxide layer, and is in good agreement with values determined by SEM (3.9 ± 0.1) μm , the micrograph of which is presented in a previous work [46]; the second (between 4.0 μm and 7.0 μm) exhibiting a gradual increase of the aluminium percentage, possibly corresponding to the interphase between the oxide layer and the substrate (clad layer); and the last, ascribed to the substrate, is characterized by a high and almost constant aluminium content. Note that the fact that the anodizing procedures were performed in as-received samples must partially explain the broad interphase between the oxide layer and the substrate. Oxygen percentages showed a quasi-spectacular behaviour in relation to aluminium, with an almost constant content in the anodizing layer, a decreasing trend at the interface between the oxide and the clad layer, and approximately constant low levels in the region corresponding to the substrate. In accordance with literature results [22,47,48], the GDOES plot in Fig. 12(a) shows the incorporation of sulphur in the anodic layer. The content increases from the bottom to the top of the anodized layer, indicating continuous incorporation of species from the electrolyte during the anodizing procedure.

The zoomed plot presented in Fig. 12(b) indicates the incorporation of Ce ions in the pores of the anodic layer. The depth profile shows slightly higher amounts on the surface of the anodized layer and at the bottom of the pores. Even though the Ce content is very low, this result must be considered relevant as no such species was detected in the depth profile of the UNS sample (plot not presented). Interestingly, a bump in the Ce amount was verified at a depth that may correspond to the lower part of the pores, indicating that Ce may have accumulated in the inner part of the porous layer (see the graphical abstract).

3.2.1.3. RBS analysis. Fig. 13 shows the experimental and simulated RBS spectra for the UNS and Ce10P 50C 2M samples. It was possible to detect Al, O and S signals in the UNS sample (Fig. 13(a)), which agrees

Table 2

Binding energies of the peaks in Fig. 9 and $\text{Ce}^{3+}/\text{Ce}^{4+}$ ratio extracted from the XPS data.

Sample/component	Ce^{3+}		Ce^{4+}		$\text{Ce}^{3+}/\text{Ce}^{4+}$						
	v_0-u_0 BE (eV)	at.%	$v'-u'$ BE (eV)	at.%	$v''-u''$ BE (eV)	at.%					
Ce10P 50C 2M	881.6–900.4	34.9	885.1–904.1	33.2	882.0–903.0	4.8	887.7–907.0	8.2	897.8–916.0	18.9	2.13

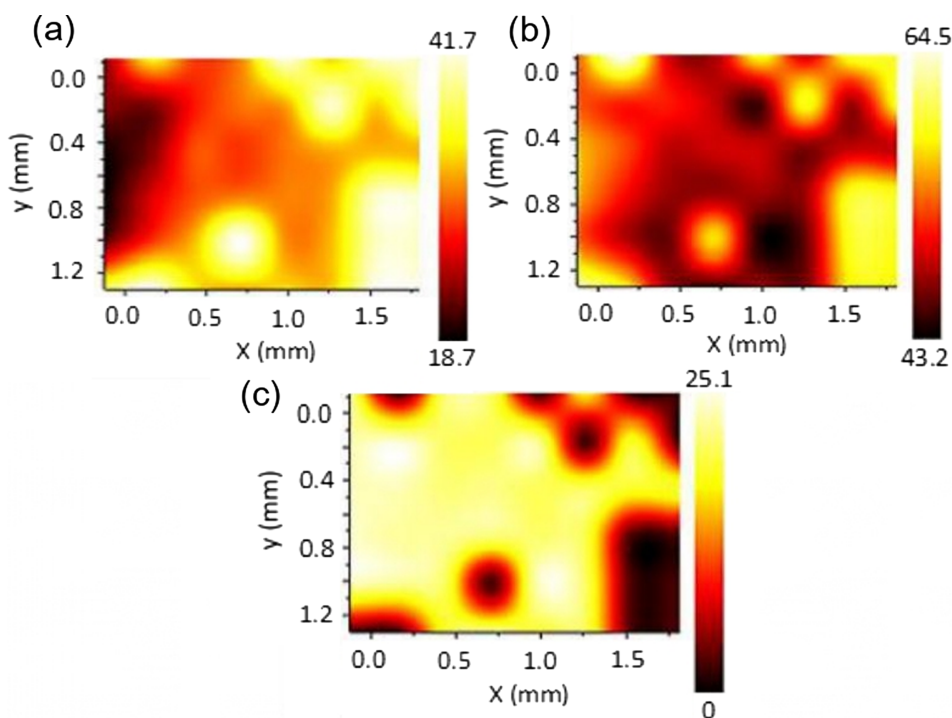


Fig. 11. XPS maps showing the atomic fractions of a) Al_{2p}; b) O_{1s} and c) Ce_{3d} on the surface of the Ce10P 50C 2M sample.

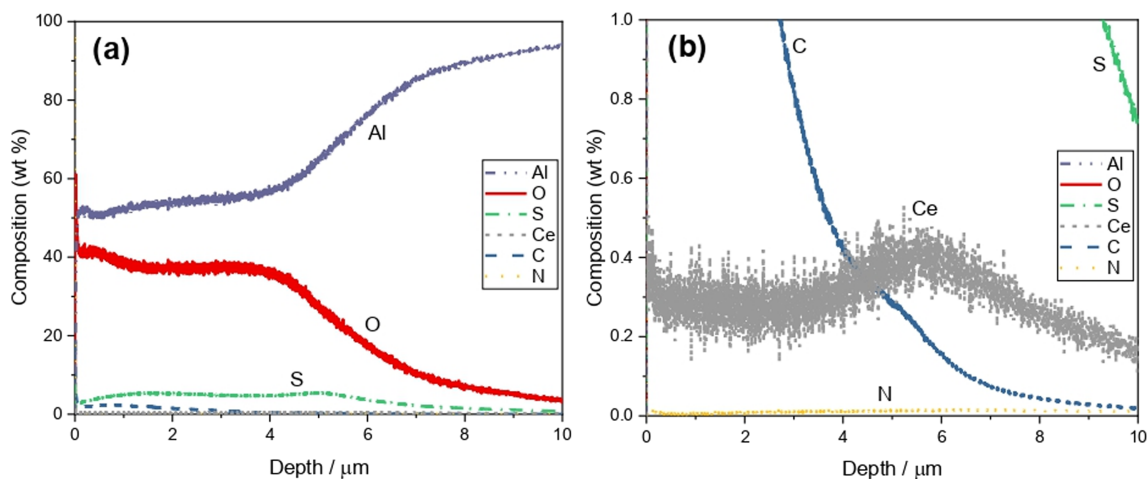


Fig. 12. (a) Glow discharge optical emission spectrometry profiles of Ce10P 50C 2M samples; (b) zoomed region of (a) evidencing Ce incorporation into the pores.

well with the composition of the anodized layer obtained by GDOES. For the Ce10P 50C 2M sample (Fig. 13(b)), the presence of signals corresponding to the incorporation of Ce into the anodized layer can be observed. These are characterized by a plateau between channels 360 and 600 and a stronger peak in channel 710. The signal between 360 and 600 refers to the Ce embedded in the pores of the anodized layer, which is in agreement with the GDOES results, while the peak on channel 710 can be assigned to Ce on the surface layer, already detected in the SEM and XPS analyses. Since Ce is the element with the largest atomic mass, the signal for the atoms on the surface appears free from the background noise produced by the other elements, as can be seen in the zoomed plot in Fig. 13 (b) [71]. For the two samples, the aluminium signal shows that the interface between the anodized and the clad layer appears approximately in channel 100, indicating that the anodized layer thickness was not modified by the post-treatment step [71]. As for the UNS sample, S and O signals were detected, but they will not be commented on, as they present the same characteristics, regardless of whether the sample was subjected to the post-treatment or not.

3.2.1.4. S/TEM – Analytical and quantitative results. A full scanning transmission electron microscopy characterization of the UNS and Ce10P 50C 2M samples was performed aiming to better evaluate the presence and distribution of Ce oxide within the pores of the anodized layer after the Ce post-treatment step.

3.2.1.4.1. Characterization of the UNS sample in the TEM mode. The microstructure of the lamella of the UNS sample after FIB is shown in the BFTEM micrograph in Fig. 14(a), where the Al alloy substrate and the anodic layer can be distinguished by their characteristic diffraction contrast. By using phase contrast (or Fresnel contrast), long vertical nanopores are visible along with the profile of the anodic layer as exhibited in the BFTEM micrographs in Fig. 14(b) and 14(c), taken respectively under and overfocus. In the underfocus condition, the nanopore walls exhibit typical bright fringes whilst in the overfocus condition, the pore walls are of a dark fringe contrast. The characterization of the nanoporosity in the anodic layer using BFTEM is similar to the characterization of voids and inert gas bubbles in solids as reported by Jenkins [72]. Using the SAED aperture as shown in the

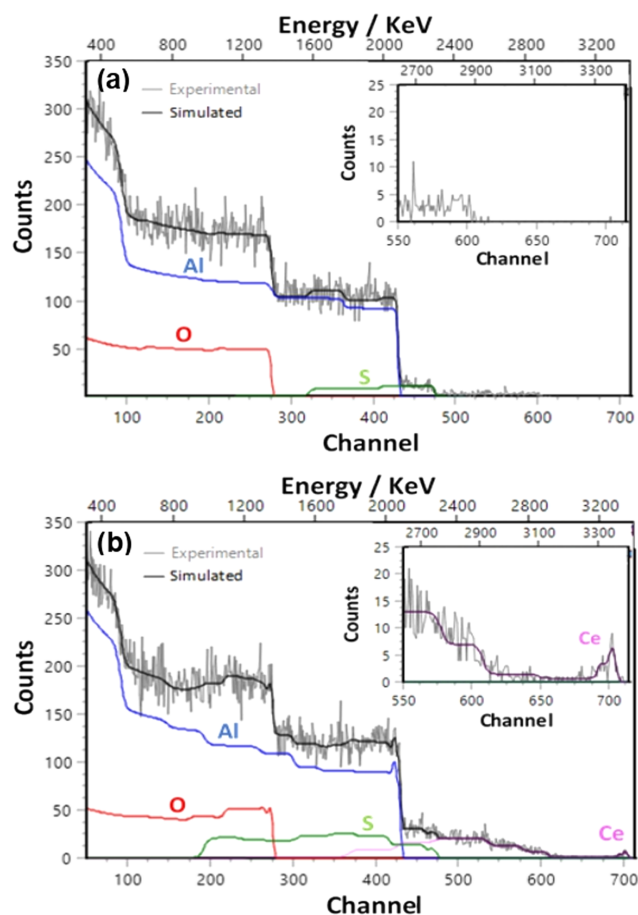


Fig. 13. RBS spectra of Alclad AA2024-T3 anodized in TSA, (a) untreated (UNS) and (b) post treated in 50 mM Ce (NO₃)₃ and H₂O₂ (10% vol) for 2 min at 50 °C (Ce10P 50C 2M).

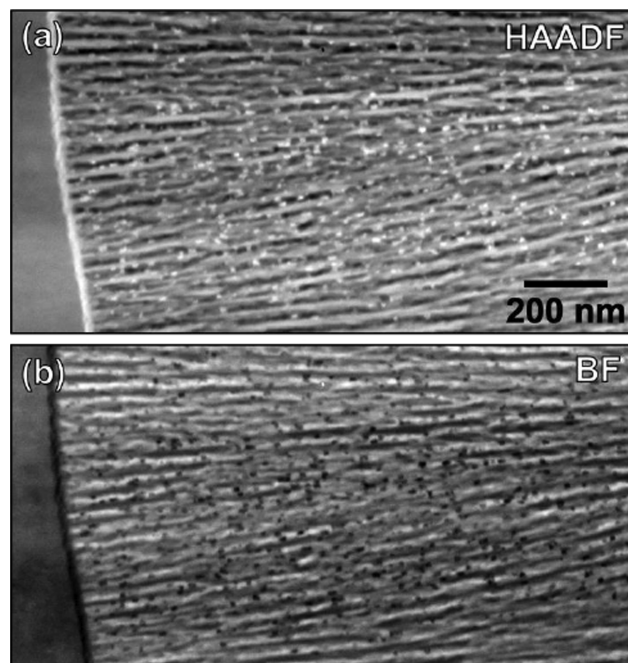


Fig. 15. HAADF and BF STEM micrographs showing the presence of nanometer-sized nanoparticles within the pores, onto the pore walls and deposited at the bottom of the pores of the Ce10P 50C 2M sample. Note: the scale bar in (a) also applies to (b).

micrograph in Fig. 14(d), an electron diffraction pattern of the anodic layer was recorded and it is confirmed that this layer is amorphous as demonstrated by the diffraction pattern in Fig. 14(e).

3.2.1.4.2. *Characterization of the Ce10P 50C 2M sample in the analytical STEM mode.* In order to investigate the anodic layer and its characteristic nanoporous structure after the post-treatment step in the Ce containing solution, STEM mode was used to characterize the cross

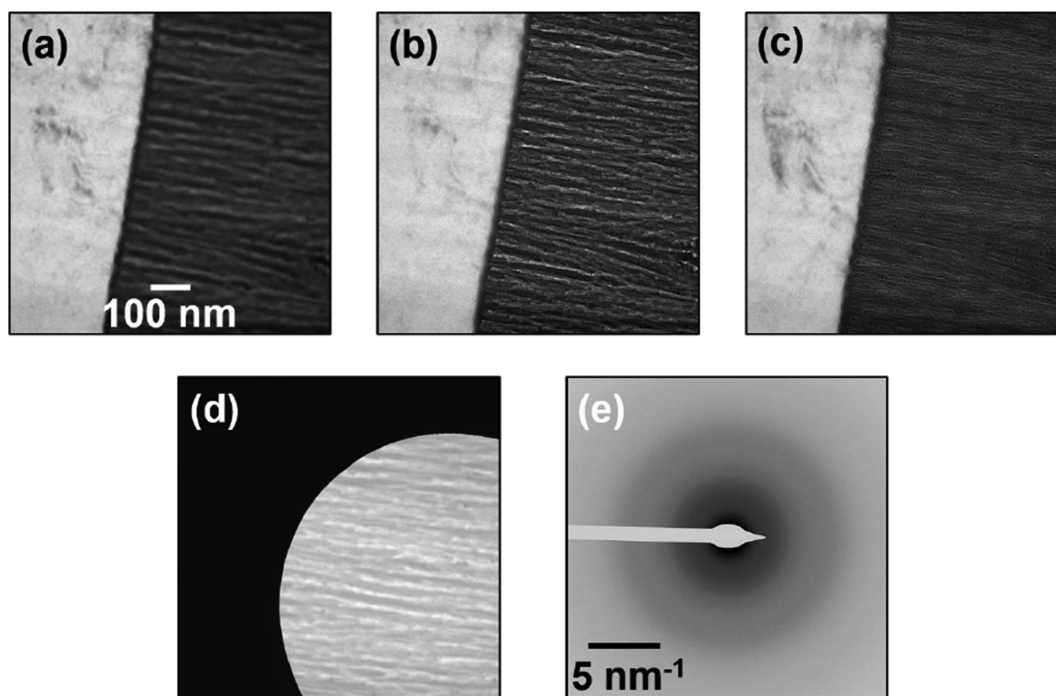


Fig. 14. TEM characterization of the anodic layer of the UNS sample. The BFTEM micrographs in (a), (b) and (c) were taken at focus, underfocus and overfocus, respectively, with a defocus of $\pm 4.9 \mu\text{m}$. The SAED micrograph in (d) was taken only in the anodic layer and its respective diffraction pattern is shown in image (e). Note: the scale bar in (a) also applies to (b-d).

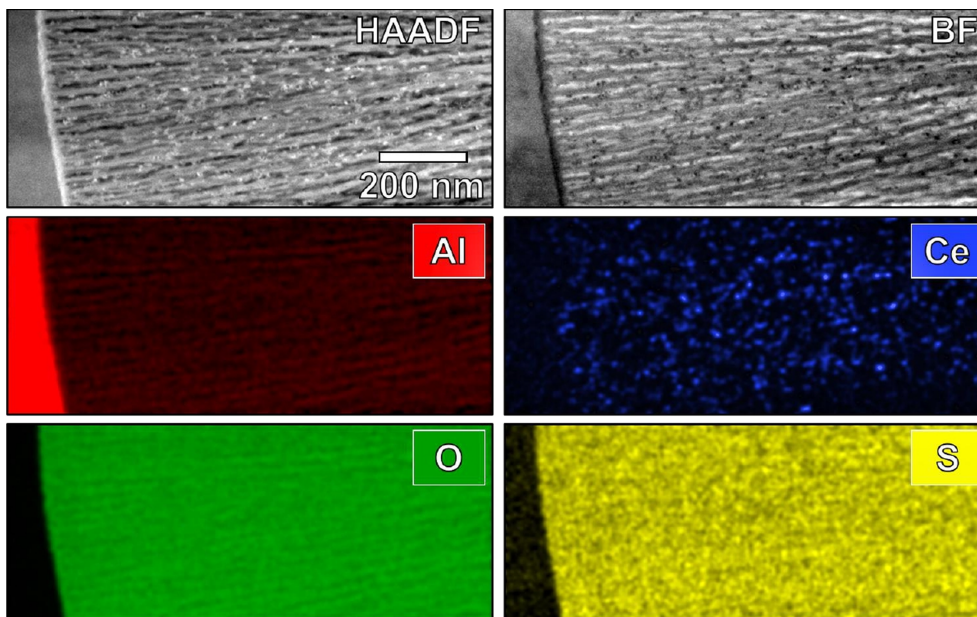


Fig. 16. STEM-EDX elemental mapping of the anodic layer of the Ce10P 50C 2M sample. The presence of Ce-containing nanoparticles was confirmed. The elemental maps were generated using the weight fraction wt.% quantification. Note: the scale bar in the HAADF image applies to all micrographs in the figure.

section of the Ce10P 50C 2M sample. As can be observed in the HAADF and BF STEM micrographs in Fig. 15(a) and 15(b), it is evident the presence of nanometer-sized round-shaped nanoparticles within the nanoporous structure of the anodic layer. In the HAADF, the nanopores have a distinct dark contrast while in BF, the nanopores are bright: this is attributed to mass thickness contrast as within the pores, there is a lack of material. As the HAADF detector is sensitive to Z-contrast (i.e. elemental composition), it is clear in Fig. 15(a) that the nanoparticles are of a different material as they are brighter than the nanopores and also their walls. The STEM micrographs of Fig. 15(a-b) also reveal that such nanoparticles are present inside the nanopores, but more prone to be stuck onto the pore walls.

STEM-EDX elemental maps were obtained with the electron-transparent lamella of the Ce10P 50C 2M sample and the results are shown in the set of images in Fig. 16. The Ce map reveals the presence of the Ce-containing nanoparticles within the anodic layer. The element S, a component of the anodizing bath, was also detected. Using the O and the Al maps, the size of the nanopores were estimated to be in the range of 10–20 nm, which is in accordance with the literature [45,47,61,73].

It is important emphasising that the microstructural characterisation of the Ce 10P 50C 2M sample within the electron microscope either on the TEM or STEM modes shows that the sample was not subjected to common FIB-induced artefacts [74], like damaging, cracks or even precipitation. This is due to the low ion beam current used in the final stages of polishing (0.5 nA to 0.1 nA) and the Pt protective layer applied prior the stages of milling and trenching.

3.2.1.4.3. Distribution of Ce-containing nanoparticles: Size and areal density. Three different areas of the anodic layer of the Ce10P 50C 2M sample were investigated using the STEM-EDX technique, thus allowing a quantification of the Ce-containing nanoparticles as shown in Fig. 17. A typical composite map containing the elements O, Al and Ce is shown in Fig. 17(a). With these three analysed areas, approximately 600 Ce-containing nanoparticles had their diameter estimated via analysis of the Ce STEM-EDX maps within the software ImageJ confirming they have an average diameter of 16.39 ± 0.04 nm as shown in the histogram in Fig. 17(b). The line profile in Fig. 17(c), corresponding to the distance marked by the black arrow in Fig. 17(a), shows that these nanoparticles have Ce enrichment. The size quantification also allowed an areal density estimation for the Ce-containing nanoparticles. The overall average areal density of the analysed sample was estimated to

be $6.1 \pm 1.9 \times 10^{10}$ nanoparticles $\cdot\text{cm}^{-2}$. This result reflects three areas measured with STEM-EDX. A trend was observed on the areal distribution of Ce-containing nanoparticles to be rather larger (~ 2.3 times larger) in the middle of the anodic layer than close to the interface with the clad substrate: at regions closer to the interface with the substrate, the average areal density was estimated to be of around $4.2 \pm 0.5 \times 10^{10}$ nanoparticles $\cdot\text{cm}^{-2}$ whereas in the middle of the anodic layer, the trend shows an areal density of around 9.9×10^{10} nanoparticles $\cdot\text{cm}^{-2}$, therefore, more than twice.

3.2.2. Analyses of corroded samples

Fig. 18 shows optical micrographs of the clad AA2024-T3 anodized in TSA after 1680 h immersion in NaCl solution (0.1 M 0–5 weeks, 0.5 M 5–10 weeks) for the conditions: (a) as-produced (UNS) and after the post-treatments Ce10P 25C 2M (b), Ce10P 50C 2M (c), Ce10P 75C 2M (d). A strong loss of brightness is observed for the UNS sample (Fig. 18(a)), indicating intense precipitation of corrosion products. In addition, this sample showed the formation of numerous pits (some selected pits are surrounded in the respective Figure), being visible at naked eye. In accordance with the EIS results, the samples post-treated for 2 min in the 50 mM cerium nitrate solution with 10% vol. of H_2O_2 showed a temperature-dependent behaviour. The Ce10P 25C 2M sample (Fig. 18(b)) showed small defects randomly distributed on the surface (one of them is indicated by the circle), while the Ce10P 75C 2M (Fig. 18(d)) showed a large amount of larger surface pits easily detectable with naked eye (some selected pits are surrounded in the respective Figure), which can be directly associated to the early drop in the BF impedance module and the layer resistance values for this latter sample, as discussed in the previous items. For the Ce10P 50C 2M sample (Fig. 18(c)), it was not possible to detect pits with naked eye, but a decrease in surface brightness was noted, indicating precipitation of corrosion products. Even so, the surface of this sample was practically intact, confirming its more stable behaviour and better resistance to corrosion as verified in the EIS tests.

Fig. 19 (a), (b) and (c) show, respectively, SEM-EDS analysis of samples UNS, Ce10P 50C 2M and Ce10P 75C 2M after 1680 h immersion in NaCl solution (0.1 M 0–5 weeks, 0.5 M 5–10 weeks). For the UNS sample, a homogeneous layer of corrosion products could be observed, with the presence of agglomerates at few sites, that can be likely associated with defective regions of the original anodized layer, as

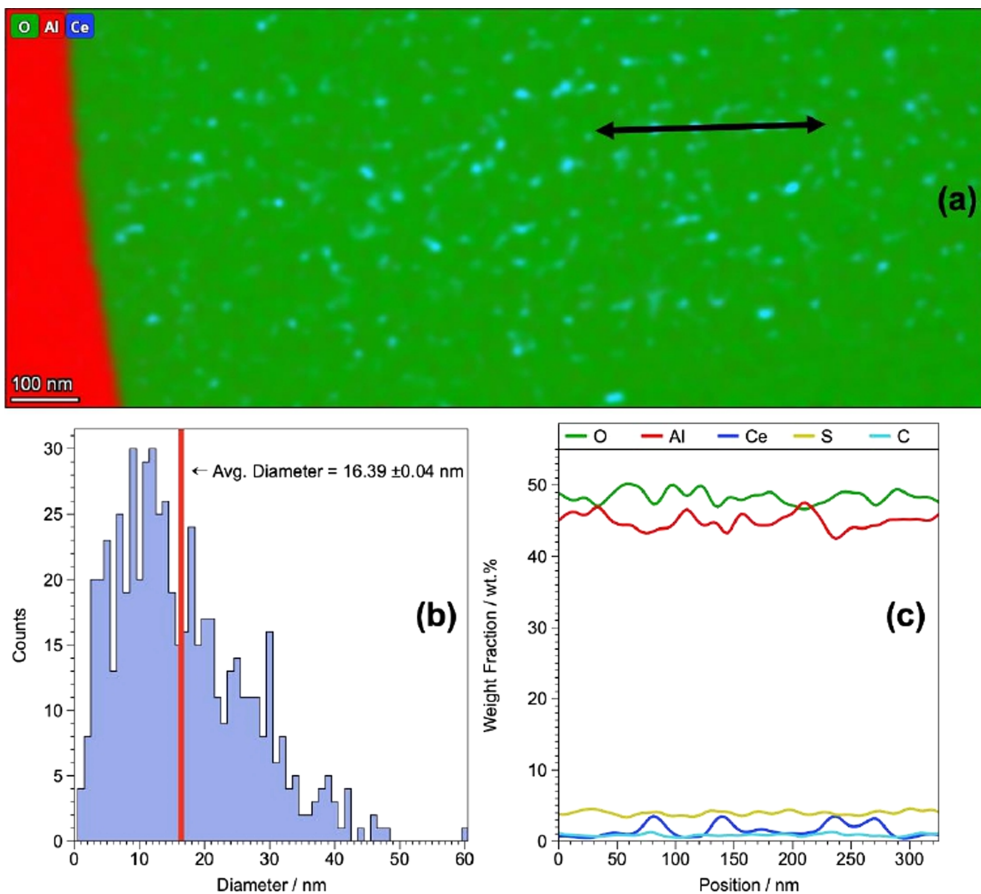


Fig. 17. Quantification of the Ce-containing nanoparticles within the anodic layer of the Ce10P 50C 2M sample. In the combined micrograph in (a), the black arrow shows the distance covered by the line profile presented in (c). The histogram of Ce-containing nanoparticles sizes in (b) was generated with approximately 600 nanoparticles measured using STEM-EDX of three different anodic layer regions.

indicated by the presence of Si in the EDS analysis (Fig. 19(a)).

The Ce10P 50C 2M sample (Fig. 19(b)) showed no signs of localized corrosion like developed pits. Nevertheless, it presented globular cerium oxide precipitates randomly distributed on the surface. The EDS

analysis of some of these sites showed the presence of Fe and Si, indicating that corrosive activity may have started or are stronger near defective regions originated by the presence of IM [15,16], the increased pH due to cathodic reaction on these sites leads to the

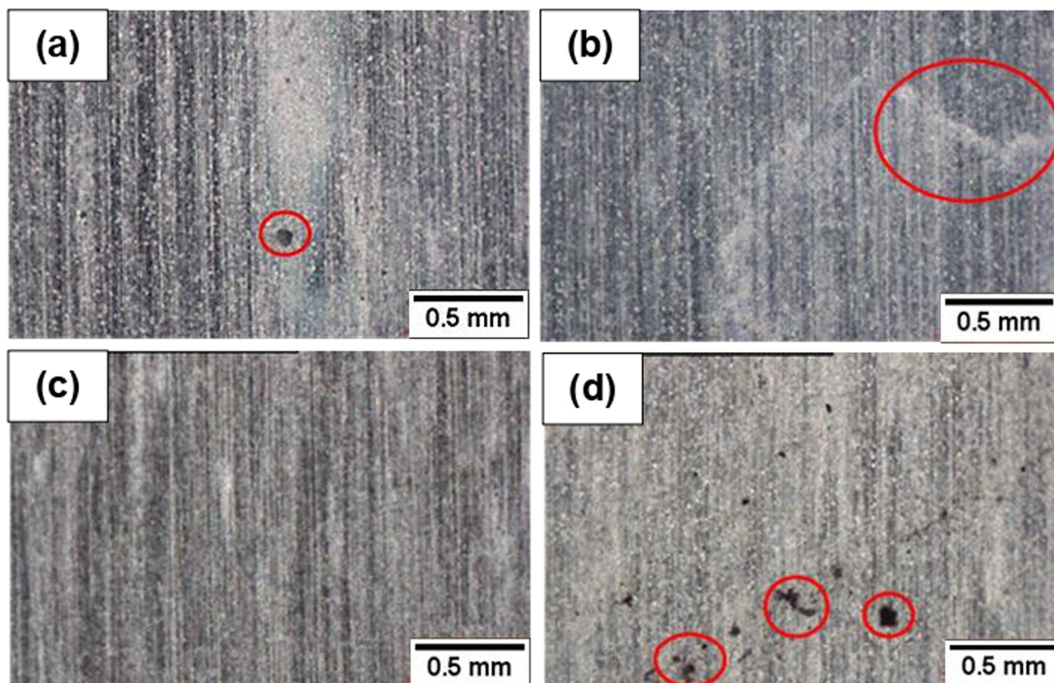


Fig. 18. Optical micrographs of the clad AA2024-T3 anodized in TSA bath after 1680 h immersion in NaCl solution (0.1 M 0–5 weeks, 0.5 M 5–10 weeks): (a) as-produced (UNS) and after post-treatments, (b) Ce10P 25C 2M, (c) Ce10P 50C 2M, (d) Ce10P 75C 2M.

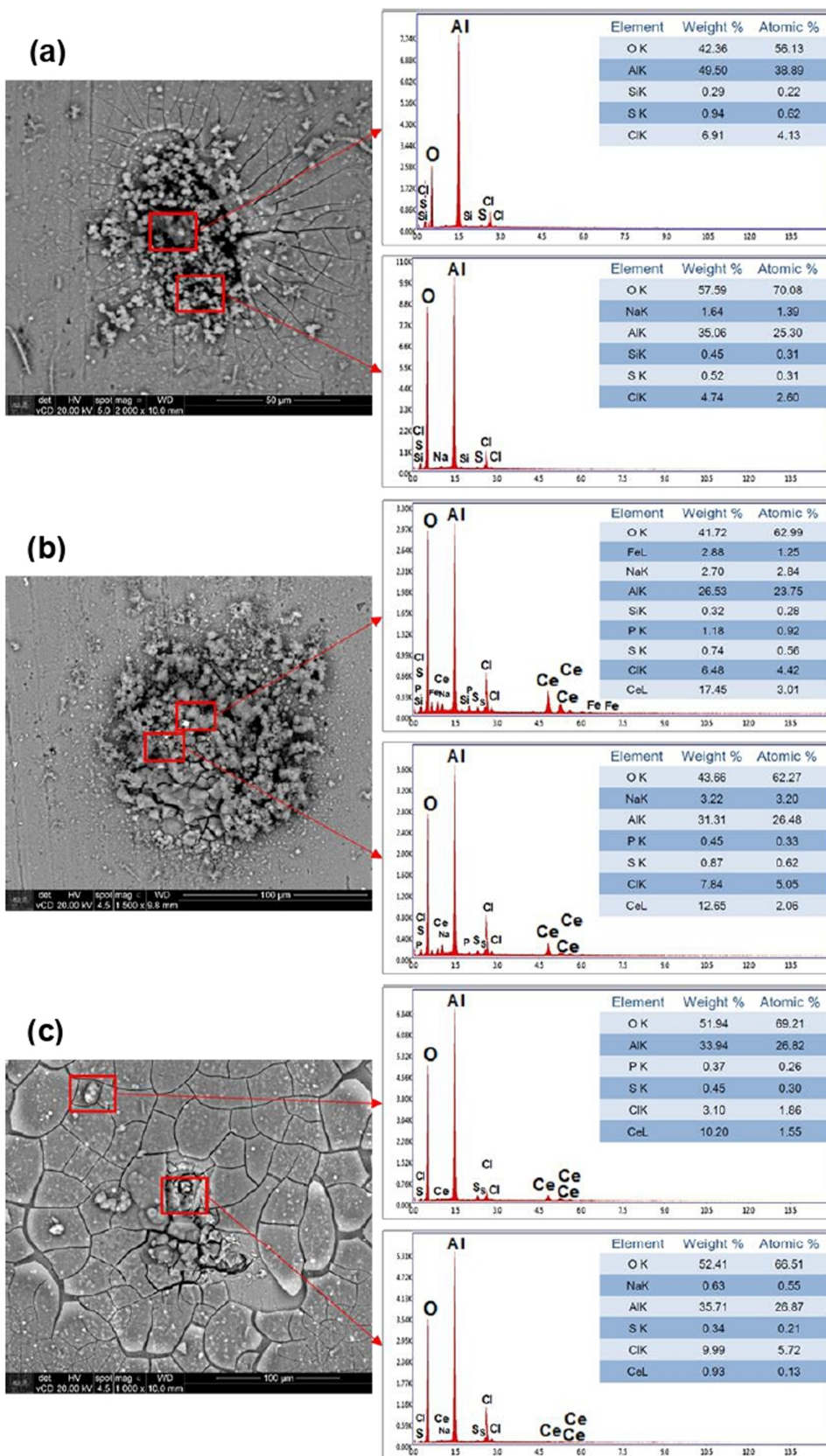


Fig. 19. SEM micrographs and EDS analyses of corrosion products on the surface of the (a) UNS, (b) Ce10P 50C 2M and (c) Ce10P 75C 2M samples after 1680 h of immersion in NaCl (0.1 M (4 h – 840 h) and 0.5 M (840 h – 1680 h)).

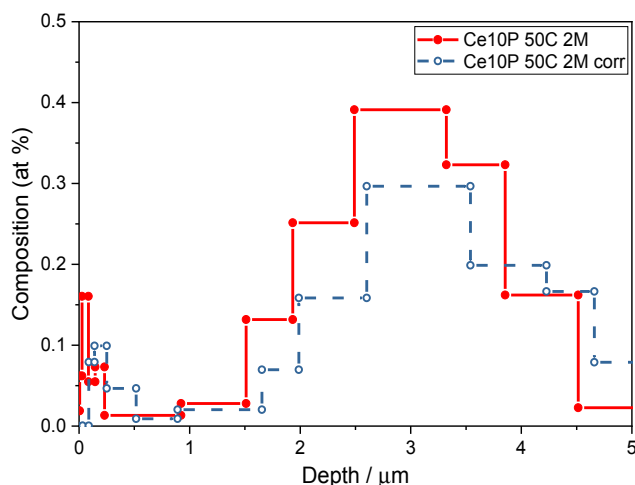


Fig. 20. Ce depth profile of Ce10P 50C 2M samples before and after 360 h (15 days) of immersion in 0.1 M NaCl, acquired by RBS.

precipitation of Ce-oxyhydroxides, possibly hindering further corrosion activity. It is worth noting that higher amounts of surface cerium oxide precipitates were observed after immersion in NaCl when compared with the as produced condition. This indicates that Ce stored in the structure of the anodized layer may be leached and precipitate on the surface of the samples when the corrosion process is triggered. For Ce10P 75C 2M sample (Fig. 19(c)), as expected, higher amounts of Ce oxide precipitates could be observed. They showed the dry mud appearance ascribed to cerium conversion layers in the literature [44,69,75], indicating its thickening, a feature not presented in the unexposed sample, reinforcing the increased precipitation of Ce compounds due to corrosion activity.

To verify if Ce ions could be retained inside the pores of the anodized layer after exposure to an aqueous electrolyte, a CeP10 50C 2M sample was immersed in 0.1 M NaCl for 360 h (15 days) and then analysed by RBS. As described in the experimental procedure, to accelerate the corrosion process, the sample was exposed horizontally. Fig. 20 presents the comparative depth profile of this sample with an unexposed one. The results show that, despite presenting a small decrease, Ce is still present in the anodized layer structure, even after a relatively long exposure period to the aggressive medium. The depth profile also indicates a stronger deposition of Ce on the surface of the anodized layer as well as at the bottom of the pores, confirming that the pores of the anodized layer may act as a nanoreservoir for Ce ions. These results are important in three aspects: first, they indicate that Ce oxyhydroxides are not easily leached by the aqueous solution, as this element continues to be detected even after 15 days of exposure of the sample to the test electrolyte without any protection; second, it proves that Ce was stably incorporated within the pores of the anodized layer; lastly, they indicate that the incorporated Ce can be progressively leached (dissolved) by the electrolyte, being able to act as a corrosion inhibitor when incorporated to a more complex protection system. Finally, it is worth mentioning that the RBS depth profiles indicate a thickness of about 4 μm for the anodized layer, which is in accordance with the GDOES determination and with our previous results published elsewhere [46].

4. Conclusions

The results of the present studies showed:

- The post-treatment of the TSA anodized layer in Ce-H₂O₂ containing solution at moderate temperature (25 °C and 50 °C) contributed to stabilizing the corrosion behaviour of the samples while maintaining the open structure of the pores. However, increasing the post-

treatment temperature to 75 °C decreased the corrosion resistance, apparently due to damages to the protective properties of both the porous and the barrier layer, as indicated by the EIS fitting procedure.

- Different characterization techniques showed the presence of Ce on the surface (SEM, XPS, GDOES and RBS) and within the pores (GDOES, RBS and S/TEM) of the anodized layer. XPS showed that Ce was present predominantly in the 3 + oxidation state, whereas GDOES and RBS showed accumulation of Ce species within the pores, a feature confirmed by S/TEM analysis, indicating that the pores of the anodized layer may provide a nanoreservoir for the Ce ions.
- Analysis of corroded samples by SEM showed an increased amount of Ce oxyhydroxides on the samples surface as compared to uncorroded species. The Ce precipitates were frequently found near defective sites of the anodized layer, indicating that Ce ions were released acting as corrosion inhibitors. For these samples, the RBS analysis showed the presence of Ce species inside the pores, even after 15 days of free exposure to the aggressive electrolyte, showing that Ce can be effectively stored within the porous structure of the anodized layer.
- S/TEM revealed Ce nanoparticles inside and attached to the pore's walls of the anodic layer.

CRediT authorship contribution statement

Oscar Mauricio Prada Ramirez: Investigation, Visualization, Writing - original draft. **Fernanda Martins Queiroz:** Conceptualization, Writing - review & editing. **Matheus Araujo Tunes:** Formal analysis, Visualization, Writing - review & editing. **Renato Albelli Antunes:** Validation, Writing - review & editing. **Cleber Lima Rodrigues:** Formal analysis, Writing - review & editing. **Alex Lanzutti:** Validation, Writing - review & editing. **Stefan Pogatscher:** Validation, Writing - review & editing. **Marie-Georges Olivier:** Supervision, Writing - review & editing. **Hercílio Gomes De Melo:** Project administration, Supervision, Writing - review & editing.

Declaration of Competing Interest

The authors declare that they have no known competing financial interests or personal relationships that could have appeared to influence the work reported in this paper.

Acknowledgements

HG de Melo is thankful to FAPESP Proc. 2018/01096-5. CNPq Proc. 400895/2014-5. O.M. Prada Ramirez is thankful to CAPES Proc. 88887.388129/2019-00. European Research Council (ERC) excellent science grant "TRANSDSIGN": Horizon 2020 program contract no. 757961. Austrian Research Promotion Agency (FFG) project 3DnanoAnalytics: contract FFG-No. 858040. MAT and SP would like to thank Francisca Mendez-Martin (Montanuniversitaet Leoben) for providing access to the Focused Ion Beam system. This study was financed in part by the Coordenação de Aperfeiçoamento de Pessoal de Nível Superior - Brasil (CAPES) - Finance Code 001.

References

- [1] N. Birbilis, R.G. Buchheit, Electrochemical characteristics of intermetallic phases in aluminum alloys, *J. Electrochem. Soc.* 152 (2005) B140–B151.
- [2] W. Zhang, G. Frankel, Transitions between pitting and intergranular corrosion in AA2024, *Electrochim. Acta* 48 (9) (2003) 1193–1210.

- [3] A. Boag, A. Hughes, A. Glenn, T. Muster, D. McCulloch, Corrosion of AA2024-T3 Part I: Localised corrosion of isolated IM particles, *Corros. Sci.* 53 (2011) 17–26.
- [4] A.E. Hughes, A. Boag, A.M. Glenn, D. McCulloch, T.H. Muster, C. Ryan, C. Luo, X. Zhou, G.E. Thompson, Corrosion of AA2024-T3 Part II: Co-operative corrosion, *Corros. Sci.* 53 (2011) 27–39.
- [5] S. Abrahami, Cr(VI)-free pre-treatments for adhesive bonding of aerospace industry, PhD Thesis, TU Delft, 2016, 183 p.
- [6] M. Kendig, S. Jeanjaquet, R. Addison, J. Waldrop, Role of hexavalent chromium in the inhibition of corrosion of aluminum alloys, *Surf. Coat. Technol.* 140 (2001) 58–66.
- [7] X. Zhao, Y. Zuo, J. Zhao, J. Xiong, Y. Tang, A study on the self-sealing process of anodic films on aluminum by EIS, *Surf. Coat. Technol.* 200 (2006) 6846–6853.
- [8] OSHA, Toxic and Hazardous Substances in Occupational Exposure to Hexavalent Chromium. (2006), United States Department of Labor; European REACH (EC n°1907/2006).
- [9] W. Lee, S. Park, Porous anodic aluminum oxide: anodization and templated synthesis of functional nanostructures, *Chem. Rev.* 114 (2014) 7487–7556.
- [10] G.E. Thompson, H. Habazaki, K. Shimizu, M. Sakairi, P. Skeldon, X. Zhou, G.C. Wood, Anodizing of aluminium alloys, *Aircraft Eng. Aerospace Technol.* 71 (1999) 228–238.
- [11] F. Mansfeld, M.W. Kendig, Evaluation of anodized aluminum surfaces with electrochemical impedance spectroscopy, *J. Electrochem. Soc.* 135 (1988) 828–833.
- [12] M. Curioni, M.S. Miera, P. Skeldon, G.E. Thompson, J. Ferguson, Macroscopic and local filming behavior of AA2024 T3 aluminum alloy during anodizing in sulfuric acid electrolyte, *J. Electrochem. Soc.* 155 (8) (2008) C387–C395.
- [13] J. Cote, E.E. Howlett, M.J. Wheeler, H.J. Lamb, The Behavior of intermetallic compounds in aluminum during sulfuric acid anodizing, Part 1: AlMn, AlFe, AlMg2Si, AlCr Alloys. *Plating* 56 (4) (1969) 386–394.
- [14] J. Cote, E.E. Howlett, H.J. Lamb, The behavior of intermetallic compounds in aluminum during sulfuric acid anodizing part 2: AlCu, AlMg, AlSi, AlTi, AlFeSi, AlZnMg Alloys. *Plating*, v. 57(5) (1970) pp. 484–496.
- [15] Y. Ma, X. Zhou, G.E. Thompson, M. Curioni, T. Hashimoto, P. Skeldon, P. Thomson, M. Fowles, Anodic film formation on AA 2099-T8 aluminum alloy in tartaric-sulfuric acid, *J. Electrochem. Soc.* 158 (2) (2011) C17–C22.
- [16] L.E. Fratila-Apachitei, J. Duszczak, L. Katgerman, Voltage transients and morphology of AlSi(Cu) anodic oxide layers formed in H₂SO₄ at low temperature, *Surf. Coat. Technol.* 157 (2002) 80–94.
- [17] Y. Ma, X. Zhou, G.E. Thompson, M. Curioni, X. Zhong, E. Koroleva, P. Skeldon, P. Thomson, M. Fowles, Discontinuities in the porous anodic film formed on AA2099-T8 aluminum alloy, *Corros. Sci.* 53 (2011) 4141–4151.
- [18] Y.T. Abrahami, J.M.M. de Kok, H. Terry, J.M.C. Mol, Towards Cr(VI)-free anodization of aluminum alloys for aerospace adhesive bonding applications: A review, *Front. Chem. Sci. Eng.* 11 (3) (2017) 465–482.
- [19] M. García-Rubio, P. Ocón, M. Curioni, G.E. Thompson, P. Skeldon, A. Lavía, I. García, Degradation of the corrosion resistance of anodic oxide films through immersion in the anodizing electrolyte, *Corros. Sci.* 52 (2010) 2219–2227.
- [20] M. García-Rubio, M.P. de Lara, P. Ocón, S. Diekhoff, M. Beneke, A. Lavía, I. García, Effect of post-treatment on the corrosion behaviour of tartaric-sulphuric anodic films, *Electrochim. Acta* 54 (2009) 4789–4800.
- [21] L. Iglesias-Rubianes, S.J. García-Vergara, P. Skeldon, G.E. Thompson, J. Ferguson, M. Beneke, Cyclic oxidation processes during anodizing of Al-Cu alloys, *Electrochim. Acta* 52 (24) (2007) 7148–7157.
- [22] M. Curioni, P. Skeldon, E. Koroleva, G.E. Thompson, J. Ferguson, Role of tartaric acid on the anodizing and corrosion behavior of AA 2024 T3 aluminum alloy, *J. Electrochem. Soc.* 156 (4) (2009) C147–C153.
- [23] M. Becker, Chromate-free chemical conversion coatings for aluminum alloys, *Corros. Rev.* 37 (4) (2019) 321–342.
- [24] B.R.W. Hinton, D.R. Arnot, N.E. Ryan, The inhibition of aluminium alloy corrosion by cerous cations, *Metals Forum* 7 (4) (1984) 211–217.
- [25] D.R. Arnot, N.E. Ryan, B.R.W. Hinton, B.A. Sexton, A.E. Hughes, Auger and XPS studies of cerium corrosion inhibition on 7075 aluminum alloy, *Appl. Surf. Sci.*, 22-23(PART 1) (1985) 236–251.
- [26] B.R.W. Hinton, D.R. Arnot, N.E. Ryan, Cerium conversion coatings for the corrosion protection of aluminium, *Metals Forum* 9 (3) (1986) 162–173.
- [27] B.R.W. Hinton, L. Wilson. A method of forming a corrosion resistant coating. *Int. Cl.* 4 C23C 22/48. WO 88/06639, September 7, 1988.
- [28] F.H. Scholes, C. Soste, A.E. Hughes, S.G. Hardin, P.R. Curtis, The role of hydrogen peroxide in the deposition of Cerium-based conversion coatings, *Appl. Surf. Sci.* 253 (4) (2006) 1770–1780.
- [29] L.M. Palomino, P.H. Suegama, I.V. Aoki, M.F. Montemor, H.G. de Melo, Electrochemical study of modified cerium-silane bi-layer on Al alloy 2024-T3, *Corros. Sci.* 51 (2009) 1238–1250.
- [30] S. Ershov, M.-E. Druart, M. Poelman, D. Cossement, R. Snyders, M.-G. Olivier, Deposition of cerium oxide thin films by reactive magnetron sputtering for the development of corrosion protective coatings, *Corros. Sci.* 75 (2013) 158–168.
- [31] G. Yoganandan, K. Pradeep Premkumar, J.N. Balaraju, Evaluation of corrosion resistance and self-healing behavior of zirconium-cerium conversion coating developed on AA2024 alloy, *Surf. Coat. Technol.* 270 (2015) 249–258.
- [32] M.F. Montemor, D.V. Snihirova, M.G. Taryba, S.V. Lamaka, I.A. Kartsonakis, A.C. Balaskas, G.C. Kordas, J. Tedim, A. Kuznetsova, M.L. Zheludkevich, M.G.S. Ferreira, Evaluation of self-healing ability in protective coatings modified with combinations of layered double hydroxides and cerium molybdate nanocontainers filled with corrosion inhibitors, *Electrochim. Acta* 60 (2012) 31–40.
- [33] K.A. Yasakau, S. Kallip, M.L. Zheludkevich, M.G.S. Ferreira, Active corrosion protection of AA2024 by sol-gel coatings with cerium molybdate nanowires, *Electrochim. Acta* 112 (2013) 236–246.
- [34] B.V. Jegdic, L.J.S. Zivkovic, J.P. Popic, J. Rogan, J.B. Bajat, V.B. Miskovic-Stankovi, Corrosion stability of cerium-doped cathaporetic epoxy coatings on AA6060 alloy, *Mater. Corros.* 67 (11) (2016) 1173–1183.
- [35] M. Dabalá, E. Ramous, M. Magrini, Corrosion resistance of cerium-based chemical conversion coatings on AA5083 aluminium alloy, *Mater. Corros.* 55 (2004) 381–386.
- [36] M. Bethencourt, F.J. Botana, M.J. Cano, R.M. Osuna, M. Marcos, Combination of thermal activation and addition of H₂O₂ to improve cerium-based immersion treatment of alloy AA5083, *Mater. Corros.* 54 (2003) 77–83.
- [37] S.V. Kozhukharov, O.F. Acuna, M.S. Machkova, V.S. Kozhukharov, Influence of buffering on the spontaneous deposition of cerium conversion coatings for corrosion protection of AA2024-T3 aluminum alloy, *J. Appl. Electrochem.* 44 (2014) 1093–1055.
- [38] B. Valdez, S. Kiyota, M. Stoytcheva, R. Zlatev, J.M. Bastidas, Cerium-based conversion coatings to improve the corrosion resistance of aluminium alloy 6061-T6, *Corros. Sci.* 87 (2014) 141–149.
- [39] S. Chen, S. Zhang, X. Ren, S. Xu, L. Yin, Cerium-based chemical conversion coating on aluminum alloy to inhibits corrosion in chloride solution, *Int. J. Electrochem. Sci.* 10 (2015) 9073–9088.
- [40] T.L. Almeida, F.M. Queiroz, M. Terada, I. Costa, V.R. Capelossi, On the effects of hydrothermal treatments on the corrosion resistance of the TSA anodized AA7475-T761 alloy, *Key Eng. Mater.* 710 (2016) 169–174.
- [41] Y. Xingwen, C. Chunan, Y. Zhiming, Application of rare earth metal salts in sealing anodized aluminum alloy, *J. Mater. Sci. Lett.* 19 (21) (2000) 1907–1908.
- [42] A. Carangelo, M. Curioni, A. Acquesta, T. Monetta, F. Bellucci, Cerium-based sealing of anodic films on AA2024T3: Effect of pore morphology on anticorrosion performance, *J. Electrochem. Soc.* 163(14) (2016) pp. C907-C916.
- [43] A. Carangelo, M. Curioni, A. Acquesta, T. Monetta, F. Bellucci, Application of EIS to in situ characterization of hydrothermal sealing of anodized aluminum alloys: comparison between hexavalent chromium-based sealing, hot water sealing and cerium-based sealing, *J. Electrochem. Soc.* 163 (10) (2016) C619–C626.
- [44] I.V. Gordovskaya, T. Hashimoto, J. Walton, M. Curioni, G.E. Thompson, P. Skeldon, Development of cerium-rich layers on anodic films formed on pure aluminium and AA7075 T6 alloy, *J. Electrochem. Soc.* 161 (14) (2014) C601–C606.
- [45] O.M. Prada Ramirez, Estudo da resistência à corrosão da liga de alumínio 2024-T3 clad anodizada em ácido tartárico sulfúrico e pós-tratada em banho contendo íons Ce, Master's dissertation presented to Polytechnic school of the University of São Paulo, São Paulo, 2019, 130 p.
- [46] O.M. Prada-Ramirez, F.M. Queiroz, M. Terada, U. Donatus, I. Costa, M.-G. Olivier, H.G. De Melo, EIS investigation of a Ce-based posttreatment step on the corrosion behaviour of Alclad AA2024 anodized in TSA, *Surf Interface Anal.*, v. 51(12) (2019) pp. 1260–1275. <https://doi.org/10.1002/sia.6633>.
- [47] V.R. Capelossi, M. Poelman, I. Recloux, R.P.B. Hernandez, H.G. de Melo, M.G. Olivier, Corrosion protection of clad 2024 aluminum alloy anodized in tartaric-sulfuric acid bath and protected with hybrid sol-gel coating, *Electrochim. Acta* 124 (2014) 69–79.
- [48] H. Costenaro, F.M. Queiroz, M. Terada, M.G. Olivier, I. Costa, H.G. de Melo, Corrosion protection of AA2524-T3 anodized in tartaric-sulfuric acid bath and protected with hybrid sol-gel coating, *Key Eng. Mater.* 710 (2016) 210–215.
- [49] T.F. Silva, C.L. Rodrigues, M. Mayer, M.V. Moro, G.F. Trindade, F.R. Aguirre, N. Added, M.A. Rizzutto, M.H. Tabacniks, MultiSIMNRA: A computational tool for self-consistent ion beam analysis using SIMNRA, *Nucl. Instrum. Methods Phys. Res., Sect. B* 371 (2016) 86, <https://doi.org/10.1016/j.nimb.2015.10.038>.
- [50] M. Mayer, Improved physics in SIMNRA 7, *Nucl. Instrum. Methods Phys. Res., Sect. B* 332 (2014) 176, <https://doi.org/10.1016/j.nimb.2014.02.056>.
- [51] L.A. Giannuzzi, F.A. Stevie, A review of focused ion beam milling techniques for TEM specimen preparation, *Micron*. 30 (1999) 197–204, [https://doi.org/10.1016/S0968-4328\(99\)00005-0](https://doi.org/10.1016/S0968-4328(99)00005-0).
- [52] J. Mayer, L.A. Giannuzzi, T. Kamino, J. Michael, TEM sample preparation and FIB-induced damage, *MRS Bull.* 32 (2007) 400–407, <https://doi.org/10.1557/mrs2007.63>.
- [53] C.A. Schneider, W.S. Rasband, K.W. Eliceiri, NIH Image to ImageJ: 25 years of image analysis, *Nat. Methods*. 9 (2012) 671–675, <https://doi.org/10.1038/nmeth.2089>.
- [54] J.A. González, V. López, A. Bautista, E. Otero, Characterization of porous aluminium oxide films from a.c. impedance measurements, *J. Appl. Electrochem.* 29 (1999) 229–238.
- [55] V. López, J.M. Bartolomé, E. Escudero, A.E. Otero, J.A. González, Comparison by SEM, TEM, and EIS of hydrothermally sealed and cold sealed aluminum anodic oxides, *J. Electrochem. Soc.* 153 (3) (2006) B75–B82.
- [56] N. Hu, X. Dong, X. He, J.F. Browning, D.W. Schaefer, Effect of sealing on the morphology of anodized aluminum oxide, *Corros. Sci.* 97 (2015) 17–24.
- [57] A. Decroly, J.P. Petitjean, Study of the deposition of cerium oxide by conversion on to aluminium alloys, *Surf. Coat. Technol.* 194 (2005) 1–9.
- [58] E. Bravo-Anagua, I.V. Aoki, Influence of cerium ions and shelf-life of hybrid solution as pretreatment for AA 2024 aluminum alloy on its anticorrosion performance, *Surf. Interface Anal.* 48 (8) (2016) 809–817.
- [59] H. Costenaro, A. Lanzutti, Y. Paint, L. Fedrizzi, M. Terada, H.G. de Melo, M.-G. Olivier, Corrosion resistance of 2524 Al alloys anodized in tartaric-sulphuric acid at different voltages and protected with a TEOS-GPTMS hybrid sol-gel coating, *Surf. Coat. Technol.* 324 (2017) 438–450.
- [60] M. Terada, F.M. Queiroz, D.B.S. Aguiar, V.H. Ayusso, H. Costenaro, M.-G. Olivier, H.G. de Melo, I. Costa, Corrosion resistance of tartaric-sulfuric acid anodized AA2024-T3 sealed with Ce and protected with hybrid sol-gel coating, *Surf. Coat. Technol.* 372 (2019) 422–426.
- [61] G. Boisier, N. Pèbère, C. Druetz, M. Villatte, S. Suel, FESEM and EIS study of sealed

- AA2024 T3 anodized in sulfuric acid electrolytes: Influence of tartaric acid, *J. Electrochem. Soc.* 155 (11) (2008) C521–C529.
- [62] J. Hitzig, K. Jüttner, W.J. Lorenz, W. Paatsch, AC - impedance measurements on porous aluminum oxide films, *Corros. Sci.* 24 (11/12) (1984) 945–952.
- [63] R. de Levie, On porous electrodes in electrolyte solutions: I. Capacitance effects, *Electrochim. Acta* 8 (1963) 751–780.
- [64] R. de Levie, On porous electrodes in electrolyte solutions-IV, *Electrochim. Acta* 9 (1964) 1231–1245.
- [65] B. Hirschorn, M.E. Orazem, B. Tribollet, V. Vivier, I. Frateur, M. Musiani, Determination of effective capacitance and film thickness from constant-phase-element parameters, *Electrochim. Acta* 55 (2010) 6218–6227.
- [66] Y.-M. Chen, A.S. Nguyen, M.E. Orazema, B. Tribollet, N. Pébère, M. Musiani, V. Vivier, Identification of resistivity distributions in dielectric layers by measurement model analysis of impedance spectroscopy, *Electrochim. Acta* 219 (2016) 312–320.
- [67] C. Lin, S. Maddela, W.G. Fahrenholtz, M.J. O'keefe, Deposition of cerium-based conversion coatings on aluminum alloy 380, *Int. J. Corrosion ID* 760284 (2012 (2012)) 9.
- [68] Y. Xingwen, L. Guoqiang, XPS study of cerium conversion coating on the anodized 2024 aluminum alloy, *J. Alloy. Compd.* 364 (2004) 193–198.
- [69] A. Uhart, J.B. Ledeuil, D. Gonbeau, J.C. Dupin, J.P. Bonino, F. Ansart, M. Esteban, An auger and XPS survey of cerium active corrosion protection for AA2024-T3 aluminum alloy, *Appl. Surf. Sci.* 390 (2016) 751–759.
- [70] K.A. Yasakau, M.L. Zheludkevich, S.V. Lamaka, M.G.S. Ferreira, Mechanism of corrosion inhibition of AA2024 by rare-earth compounds, *J. Phys. Chem. B* 110 (2006) 5515–5528.
- [71] M. García-Rubio, P. Ocón, A. Climent-Font, R.W. Smith, M. Curioni, G.E. Thompson, P. Skeldon, A. Lavia, I. García, Influence of molybdate species on the tartaric acid/sulphuric acid anodic films grown on AA2024 T3 aerospace alloy, *Corros. Sci.* 51 (2009) 2034–2042.
- [72] M.L. Jenkins, Characterisation of radiation-damage microstructures by TEM, *J. Nucl. Mater.* 216 (1994) 124–156, [https://doi.org/10.1016/0022-3115\(94\)90010-8](https://doi.org/10.1016/0022-3115(94)90010-8).
- [73] L. González-Rovira, L. González-Souto, P.J. Astola, C. Bravo-Benítez, F.J. Botana, Assessment of the corrosion resistance of self-ordered anodic aluminum oxide (AAO) obtained in tartaric-sulfuric acid (TSA), *Surf. Coat. Technol.* 399 (2020) 126131.
- [74] N.I. Kato, Reducing focused ion beam damage to transmission electron microscopy samples, *J. Electron Microsc.* 53 (5) (2004) 451–458.
- [75] M. Dabalà, L. Armelao, A. Buchberger, I. Calliari, Cerium-based conversion layers on aluminum alloys, *Appl. Surf. Sci.* 172 (2001) 312–322.